Heat Transport in Silicon Nitride Drum Resonators and its Influence on Thermal Fluctuation-induced Frequency Noise

Nikaya Snell

Thesis submitted to the University of Ottawa
in partial fulfillment of the requirements for the degree of

MASTER OF APPLIED SCIENCE

Department of Mechanical Engineering
Faculty of Engineering
University of Ottawa

Abstract

Silicon nitride (SiN) drumhead resonators offer a promising avenue for thermal sensing due to their high mechanical quality factor and the high temperature sensitivity of their resonance frequency. As such, gaining an understanding of heat transport in SiN resonators as well as their sensing noise limitations is of interest, which are the two goals of the present work. We first present new experimental results on radiative heat transport in SiN membrane, which we use for benchmarking two recently proposed theoretical models. We measure the characteristic thermal response time of square SiN membranes with a thickness of 90 ± 1.7 nm and side lengths from 1.5 to 12 mm. A clear transition between radiation and conduction dominated heat transport is measured, in close correspondence with theory. In the second portion of this work, we use our experimentally validated heat transport model to provide a closed-form expression for thermal fluctuation-induced frequency noise in SiN membrane resonators. We find that, for large area SiN membranes, thermal fluctuations can be greater than thermomechanical contributions to frequency noise. For the specific case of thermal radiation sensing applications, we also derive the noise equivalent power resulting from thermal fluctuation-induced frequency noise, and we show in which conditions it reduces to the classical detectivity limit of thermal radiation sensors. Our work therefore provides a path towards achieving thermal radiation sensors operating at the never attained fundamental detectivity limit of bolometric sensing. We also identify questions that remain when attempting to push the limits of bolometric sensing, in particular, the effect of thermal fluctuation noise in closed-loop frequency tracking schemes remain to be clarified.

Thesis structure

This thesis builds in large part from a scientific article that is being submitted simultaneously for publication. Chapters 1 and 2 of this thesis present extended literature review and background information that are not included in the article, while the following chapters are taken almost entirely from the article preprint. The original article preprint can be accessed at https://arxiv.org/abs/2110.00080 and is also provided in appendix.

Table of Contents

List of Figures

1. Introduction

1.1 Nanomechanical Thermal Radiation Sensors

Due to their operating principles, traditional thermal detectors, such as the one shown below in Figure 1.1, operate far above the fundamental limit (i.e., the limit imposed by thermal fluctuation noise). With traditional detectors, when the absorptive material is heated by incident radiation the increase in temperature is measured via an electrical signal, such as voltage or resistance. This method of detection causes traditional thermal detectors to be limited by electrical noise, also known as Johnson noise.

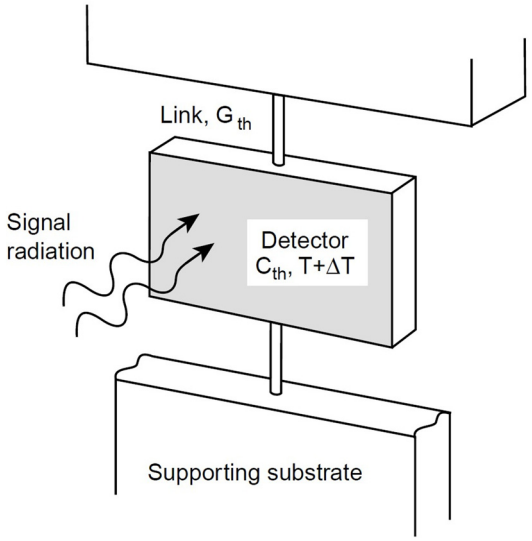

Figure 1.1. Schematic of a traditional thermal infrared detector [1].

The use of nanomechanical resonators offers a promising avenue for improving the performance of infrared thermal by reducing and even eliminating Johnson noise [2]–[8]. More precisely, the use of silicon nitride (SiN) nano/micro-mechanical resonators (NEMS/MEMS) in thermal sensing schemes is especially appealing due to the ability to form high quality factor resonators whose resonance frequency is highly sensitive to temperature changes [3], [4], [9]–[11]. Using a SiN drumhead resonator (Figure 1.2 a), the changes in

resonance frequency can be induced by incident infrared radiation (Figure 1.2 b) and in turn measured using an optical readout system, such as an interferometer, which is the basis for the experiments performed in this work.

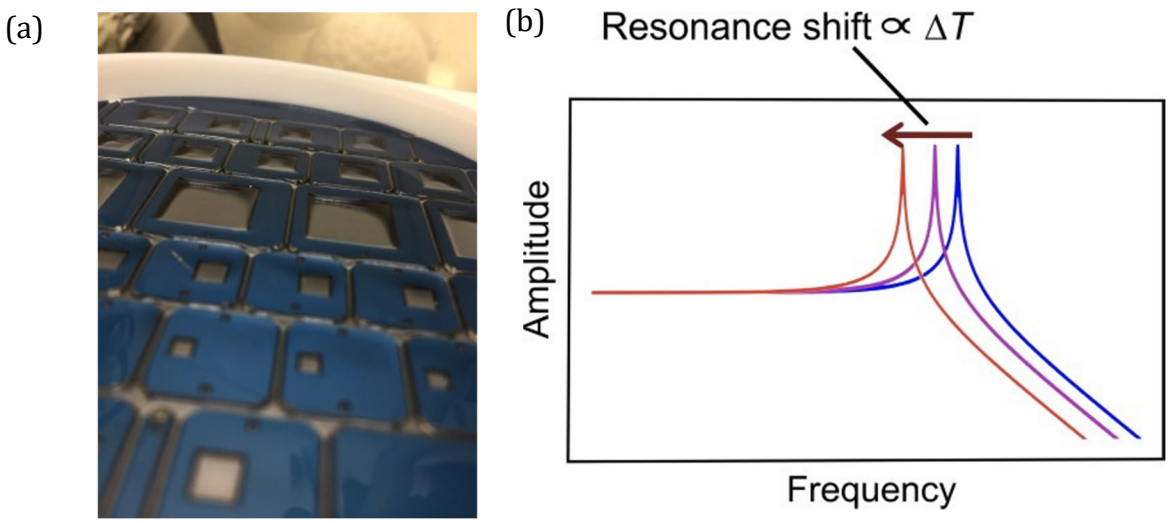

Figure 1.2. (a) SiN drumhead resonators during etching in potassium hydroxide (KOH) *solution. (b) Resonance frequency shift due to temperature change.*

1.2 Objective/Scope of this Work

To further the development of SiN thermal sensors, there has been recent interest in understanding the radiative and conductive heat transport in SiN membranes [4], [11]–[13] . Recent studies [4], [11], including one by our group [4], proposed models for thermal radiation heat transport in square silicon nitride membranes using either a circular approximation [4] or a first-order Taylor expansion approximation [11]. A distinctive feature of the work in our lab [4] was the inclusion an analytical model for the emissivity of SiN. On the other hand, experimental validation of our model was only preliminary. A single membrane size was tested experimentally using a continuous-wave IR radiator, whose static nature resulted in relatively large uncertainties due to drift. In [11], a first order Taylor model corresponded well with experimental measurements for 50 nm thick square membranes. Dynamic measurements were performed for various membranes side-lengths up to 4 mm, for which the fraction of heat transfer occurring by radiation (x_{rad}) is predicted to be

approximately 70% [4], i.e., where 30% of the total heat transfer still occurs via conduction. Despite this conclusive demonstration, observation of a fully radiation-dominated region is still desirable. This would notably allow a more direct confirmation of existing models [4], [14] and measurements [11] on the emissivity of SiN.

The goal of this work is two-fold. First, additional experimental validation is provided for these models by performing dynamic measurements of the thermal response time of SiN membranes for membrane sizes up to 12 mm. A clear region of radiation-dominated heat transport ($x_{rad} \approx 90\%$) is observed, which allows for a detailed comparison with recently proposed models for thermal transport [4], [11], emissivity [4], [14], and thermal conductivity [12], [13], [15].

Secondly, the validated model for heat transport is used to derive a closed-form expression for thermal fluctuation-induced frequency noise in drum resonator-based radiation sensors. Using this model, it can be shown that thermal fluctuation noise can potentially dominate over thermomechanical frequency noise in large area SiN. This outlines the importance of considering thermal fluctuation noise together with other noise sources (i.e., thermomechanical and detection noise) within recently proposed frameworks for frequency noise in nanomechanical resonators [16]–[20].

2. Literature Review

2.1 Fundamental Limit of Bolometers

Traditional bolometers, such as the one shown in Figure 1.1, are unable to reach the fundamental limit of thermal detectors due to being limited by Johnson noise owing to their use of an electrical readout system. In Figure 2.1, a common performance metric of detectors, the specific detectivity, is shown for various commercially available radiation detectors along with the fundamental limit for thermal detectors (green dashed line in Figure 2.1). With specific detectivity being defined as the inverse of noise equivalent power (NEP) normalized by area, a higher detectivity equates to a better radiation detector. The performance limit of bolometers (blue dashed line in Figure 2.1) is $\sim 2 \times 10^8\ cm\sqrt{Hz}/W$ and is notably two orders of magnitude below the fundamental limit ($\sim 2 \times 10^{10}\ cm\sqrt{Hz}/W$) of thermal detectors.

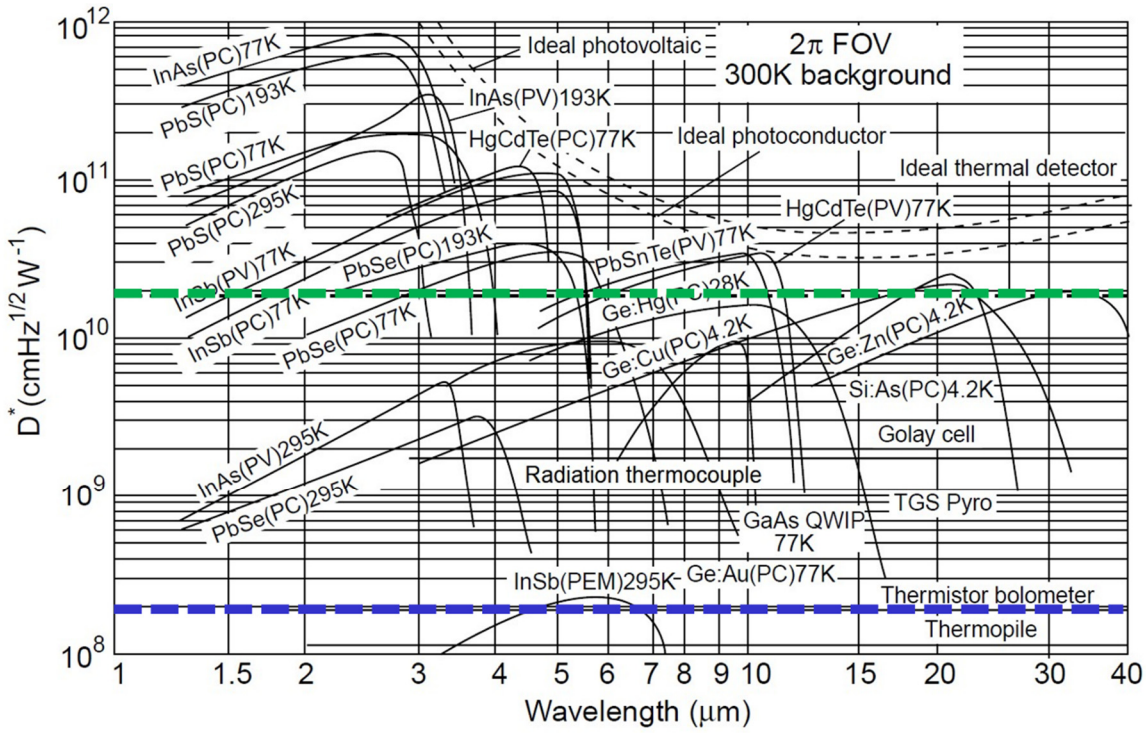

Figure 2.1. Specific detectivity of various radiation detectors [1]. Green dashed line represents the fundamental limit of thermal detectors while the blue dashed line represents specific detectivity of traditional bolometers.

It should be noted that photon detectors are able to achieve detectivities higher than the limit of thermal detectors, however, there are drawbacks to this other type of radiation sensor. While photon detectors boast a high signal to noise ratio and fast response, the drawback of photon detectors is their increased cost and impracticality for many applications due to needing to be cryogenically cooled. In contrast, thermal detectors are able to operate at room temperature and are more cost effective thus lending to the need to close the performance gap between current technology and the fundamental detectivity limit of thermal detectors.

This literature review is broken up into three main sections. First, various types of frequency noise present in nanomechanical resonators are defined to better understand the factors limiting thermal radiation detectors from being dominated by thermal fluctuation induced noise and reaching the fundamental limit. After understanding potential sources of noise, current works on nanomechanical thermal detectors are reviewed and the current limitations are identified. Following this, the methods by which heat transfer in nanomechanical resonators are modeled are introduced.

2.2 Noise in NEMS/MEMS

This section outlines commonly considered sources of noise in resonance-shift based nanomechanical sensors. Before delving into the different sources of noise, it is important to understand how noise can be quantized in nanomechanical resonators. Two main metrics that will be reviewed in this section are spectral density and Allan deviation.

Power spectral densities (PSD) allow analysis of the intensity of frequency or phase noise as a function of Fourier frequency [21]. The typical notation for a power spectral density of fractional frequency fluctuations is S_y and the units are $1/Hz$. Spectral density terms exist for specific sources of noise, such as temperature spectral density ($S_T(\omega)$ in K^2/Hz) for thermal noise and thermomechanical spectral density ($S_x(\omega)$ in m^2/Hz); however these spectral density terms are difficult to compare whereas the use of a PSD of fractional frequency

fluctuations allows comparison of different noise sources while still maintaining a relation to the underlying noise process.

The Allan variance is another useful noise analysis tool and is a metric for defining the stability of an oscillator vibrating at a specific resonance frequency. Allan variance can be expressed as [22], [23]:

$$\sigma_{AV}^2(\tau) = \frac{1}{2(N-1)} \sum_{i=1}^{N-1} \left(\frac{\bar{f}_{i+1} - \bar{f}_i}{f_o} \right)^2 \tag{2.1}$$

where N is the number of samples at a given resonance frequency, f_o is the desired resonance frequency of the oscillator, and $\bar{f}_i$ are samples of the resonance frequency averaged over an integration time τ. Allan variance is also commonly expressed as a deviation, wherein the square root of the variance is taken ($\sqrt{\sigma_{AV}^2}$). It is also possible to convert between spectral densities and Allan deviations using the following equation [21]:

$$\sigma_{AV}^2(\tau) = \int_0^{f_c} S_y(f) \left| 2 \left(\frac{\sin(\pi\tau f)}{\pi\tau f} \right)^2 \sin^2(\pi\tau f) \right|, \tag{2.3}$$

Make use of either the Allan deviation or variance allows the sources of frequency noise to be easily identified as white noise, 1/f noise, or drift as seen in Figure 2.2. White noise can be decreased as the Allan deviation integration time (τ) is increased. Conversely, increasing the integration time (τ) has no effect on 1/f noise and results in an increase is noise due to drift. Models for predicting the Allan deviation of different sources of noise in nanomechanical resonators are prevalent in literature and will be defined in the following sub-sections.

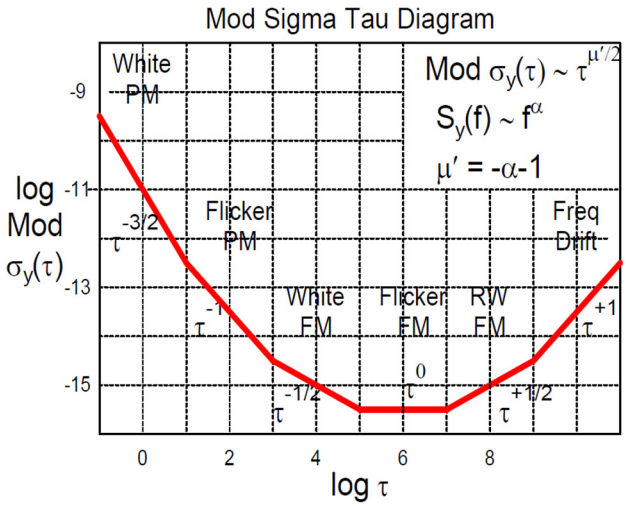

Figure 2.2. Frequency fluctuation classifications in Allan variance [21].

Another useful metric for defining frequency noise is noise equivalent power (NEP), which can be defined as signal power required to obtain a signal to noise ratio of one over a given bandwidth (i.e., the minimum detectable power). However, closed formed expressions of NEP for different types of frequency noise (e.g., thermomechanical, thermal, etc.) are often not given in literature. As such, equations for this metric have not been included in this literature review; however, it is possible to convert Allan deviation values to NEP [24]:

$$NEP = \frac{\sigma_{AD}\sqrt{\tau}}{R}, \tag{2.4}$$

where R is the responsivity of the resonator, which can be defined as the resonator's change in resonance frequency due to a given stimulus (e.g., radiation, mass, etc.).

2.2.1 Thermomechanical Noise

Thermomechanical noise is a white noise source that is the result of random thermal excitation of particles around and within a nanomechanical resonator [19], [20], [25], [26]. Since this source of noise is proportional to the mass and quality factor of a resonator, working at smaller dimensions increases the contribution of thermomechanical noise to the overall system noise. It is often the limiting noise source in NEMS/MEMS despite techniques

such as performing experiments in vacuum to minimize the presence of particles around the resonator [5], [16]–[18], [25].

The most simplified expression for thermomechanical noise as a white spectral density is the following [16], [17]:

$$S_{y,tmech}(\omega) = \frac{k_B T}{m_{eff}\omega_r^3 Q a_{rss}^2}, \tag{2.5}$$

where k_b is the Boltzmann constant, T is temperature in K, m_{eff} is the effective mass of the resonator, ω_r is the angular resonance frequency of the resonator, Q is the quality factor of the resonator, and a_{rss} is the steady state amplitude of the resonator. Taking a closer look at the parameters defined in the above equation further emphasizes the effect mass reduction has on thermomechanical noise. It is also possible to see that selecting higher order modes (and thus a higher resonance frequency), using a resonator with a high quality factor, and increasing the vibration amplitude of the resonator can all contribute to minimization of thermomechanical noise.

Thermomechanical noise can also be expressed as an Allan deviation [18]:

$$\sigma_{AD,tmech}(\tau) = \frac{1}{2Q}\frac{N_{tmech}}{a_{rss}}\sqrt{\frac{1}{\tau}} = \frac{1}{2Qa_{rss}}\sqrt{\frac{k_b T Q}{2\pi^3 m_{eff} f_r^3}}\sqrt{\frac{1}{\tau}}, \tag{2.6}$$

where N_{tmech} is the noise level in $m/\sqrt{Hz}$ and f_r is the resonance frequency in Hz. The above expression gives a white noise asymptote, as seen in Figure 2.2, for the thermomechanical induced frequency noise of the resonator.

2.2.2 Detection Noise

Detection noise is a term that encompasses the conversion of resonator displacement into optical or electrical signals, any signal amplification, and the system readout [16]. The spectral density of this noise source can be expressed as

$$S_{y,det}(\omega) = \kappa_d^2 \frac{k_B T}{m_{eff}\omega_r^3 Q a_{rss}^2}, \tag{2.7}$$

where κ_d is a dimensionless scaling parameter that indicates whether thermomechanical noise can be resolved above the detection noise of the system. The scaling parameter κ_d must be determined experimentally by comparing the PSD due to thermomechanical noise to the baseline PSD of the system [18].

Similar to thermomechanical noise, detection noise is another white noise source in the system. This means that increasing the Allan deviation averaging time results in a decrease in the level of detection noise. The Allan deviation for detection noise is [18]

$$\sigma_{AD,tmech}(\tau) = \frac{1}{2Q}\frac{N_{\text{det}}}{a_{rss}}\sqrt{\frac{1}{\tau}}, \tag{2.8}$$

where N_{det} is the noise level in $V/\sqrt{Hz}$.

2.2.3 Thermal Fluctuation Noise

Thermal fluctuation noise is caused by energy exchanges between the resonator material and its surrounding environment. These exchanges affect the temperature of the nanomechanical resonator [2], which are especially sensitive due to their small geometries and limited heat capacities, resulting in resonance frequency shifts. To reach the fundamental limit of thermal radiation sensors, thermal fluctuation induced frequency noise must be the dominating source of noise in the system [1].

Often thermal fluctuation noise is expressed as a temperature spectral density with units K^2/Hz [2], [19], [20]:

$$S_T(\omega) = \frac{4k_B T^2}{G}\frac{1}{1+\omega^2\tau_{th}^2}, \tag{2.9}$$

where G is the thermal conductance of the resonator in W/K and τ_{th} is the characteristic thermal time constant of the resonator in s. This can be converted into a spectral density using the sensitivity (α) of the resonator in Hz/K and resonance frequency (f_r) in Hz:

$$S_y(\omega) = S_T(\omega)\frac{\alpha^2}{f_r^2}, \tag{2.10}$$

Thermal fluctuation noise is often neglected when performing noise analysis in favour of modelling thermomechanical noise and detection noise, which typically dominate [16]–[18], [25]. As such general expressions for the thermal Allan deviation (i.e., expressions that are not linked to a specific resonator geometry as in [20]) are often not included in literature. As a result, the Allan deviation for thermal fluctuation noise is best expressed by converting the spectral density in Eq. (2.10) to an Allan deviation using Eq. (2.3)

$$\sigma_{AD}(\tau) = \left[\int_0^{f_c} \frac{4k_B T^2}{G}\frac{1}{1+\omega^2\tau_{th}^2}\frac{\alpha^2}{f_r^2}\left|2\left(\frac{\sin(\pi\tau f)}{\pi\tau f}\right)^2 \sin^2(\pi\tau f)\right|\right]^{1/2}, \tag{2.11}$$

2.2.4 Other Sources of Noise

The sources of noise discussed in this section are negligible due to their low magnitude in most works on thermal radiation detectors based on nanomechanical resonator. These noise sources include adsorption/desorption noise and diffusion noise. In Figure 2.3, the small contribution adsorption/desorption and diffusion noise have in comparison to the typical frequency stability of a resonator is shown. It can be seen that adsorption/desorption noise is ~5 orders of magnitude below the experimental Allan deviation, while diffusion noise is significantly lower at ~14 orders of magnitude below experimental values.

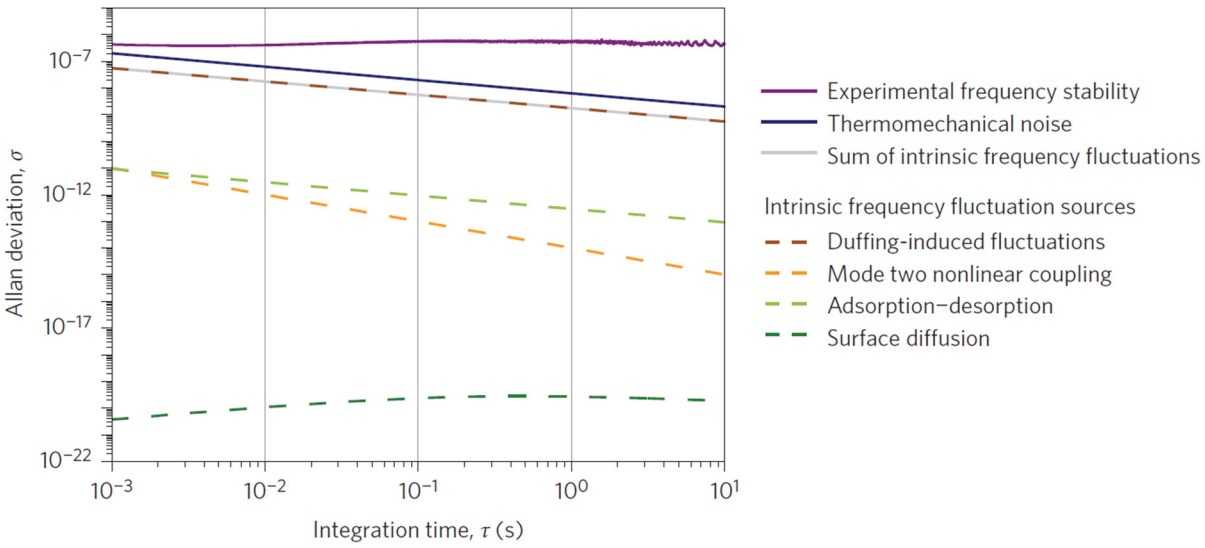

Figure 2.3. Allan deviation showing magnitude of adsorption/desorption noise and diffusion noise in comparison to typically dominating noise sources. Taken from [25].

Adsorption/Desorption Noise

Adsorption/desorption noise is a result of a change in resonance frequency due to molecules attaching to the surface of the resonator [19], [20], [25], [27], [28]. The Allan deviation of noise resulting from mass loading caused by adsorption/desorption is [20], [25]

$$\sigma_{AD}(\tau) = \frac{1}{2\sqrt{3}}\sigma_{occ}\sqrt{N_a}\left(\frac{m_{mol}}{m_{res}}\right)\left(\frac{\tau_r}{\tau}\right)^{\frac{1}{2}}, \tag{2.12}$$

where $\sigma_{occ} = \sqrt{r_a r_d}/(r_a + r_d)$ is the deviation in occupation probability, $N_a$is the number of adsorption/desorption sites on the resonator, m_{mol} is the mass of the binding molecule, m_{res} is the mass of the resonator, and $\tau_r = 1/(r_a + r_d)$ is the correlation time of an adsorption/desorption cycle. The adsorption rate (r_a) and the desorption rate (r_d) are [20], [25]

$$r_a = \frac{2}{5}\frac{P}{\sqrt{m_{mol}k_bT}}s, \tag{2.13}$$

$$r_d = \nu_d \exp\left(-\frac{E_b}{k_b T}\right), \tag{2.14}$$

where P is pressure, s is a temperature dependent sticking coefficient, ν_d is the desorption attempt rate, E_b is the energy necessary for desorption to occur. Another means of expressing adsorption/desorption noise is as a spectral density:

$$S_y(\omega) = \frac{N_a \sigma_{occ}^2 \tau_r}{2\pi(1+\omega^2\tau_r^2)}\left(\frac{m_{mol}}{m_{res}}\right)^2, \tag{2.15}$$

In the figure below the Allan variance due to adsorption/desorption for a resonator at different temperatures is shown to help visualize parameters that can minimize this source of noise. Here it is possible to see that increasing the temperature of the resonator causes the Allan variance to decrease since the resonator mass remains more consistent due to a reduction in the adsorption/desorption rate of particles (see Eq. 2.10 – 2.11). Figure 2.4 also shows that reducing the ambient pressure, for example by performing experiments in a vacuum, helps minimize adsorption noise by reducing the rate particles attach to the resonator. Another potential means of minimizing this source of noise, which is not evident in the figure below, is to functionalize the surface of the resonator to reduce the sticking coefficient (s) [20].

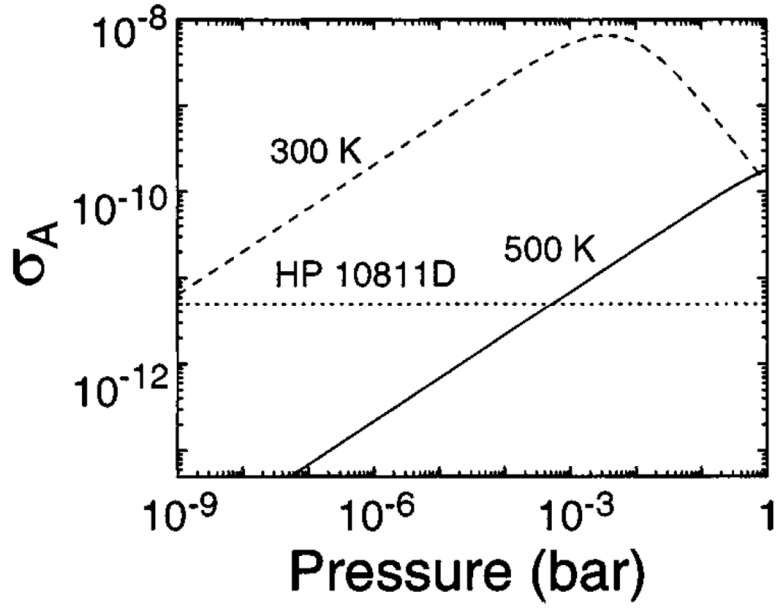

Figure 2.4. Allan variance (τ = 1 s) as a function of pressure for resonators at 300 K and 500 K.

Diffusion Noise

Diffusion noise is closely linked to adsorption/desorption noise as it is caused by a change in the mass distribution of the resonator due to the motion of particles attached to the resonator surface [25], [28]. Variations in the mass distribution of the resonator lead to a change in resonance frequency. In terms of an Allan deviation, diffusion can be expressed as [25], [28]

$$\sigma_{AD}(\tau) \approx 0.83\sqrt{N}\left(\frac{m_{mol}}{m_{res}}\right)\left(\frac{\tau_D}{\tau}\right)^{\frac{1}{4}}, \tag{2.16}$$

for the case where the time constant of the diffusion process, τ_D, is much smaller than the integration time (i.e., a slow measurement). In the above equation, N is the number of particles on the surface, which is essentially the number of adsorption sites (N_a) that are occupied. In low pressure applications, the number of adsorption sites that are occupied is minimal thus contributing to the small magnitude of diffusion noise seen in Figure 2.3. The

second case to consider is when there is a fast Allan deviation measurement ($\tau \ll \tau_D$) [25], [28]

$$\sigma_{AD}(\tau) \approx 0.51\sqrt{N}\left(\frac{m_{mol}}{m_{res}}\right)\left(\frac{\tau_D}{\tau}\right)^{\frac{1}{2}}, \tag{2.17}$$

2.2.5 Loop Dynamics

Previous sections have largely neglected the effect frequency tracking schemes have on overall system noise. In essence, the previous sections have assumed that resonators are operating in an open-loop scheme as seen in Figure 2.5 (a). This is often not the case, as experiments often incorporate a phase locked loop (PLL) to track the resonance frequency of the resonator in a closed loop scheme (Figure 2.5 b). Integrating this sort of frequency tracking scheme results in a trade-off, the speed of measurements can be increased through the use of a PLL at the expense of increased noise in the system [16], [18].

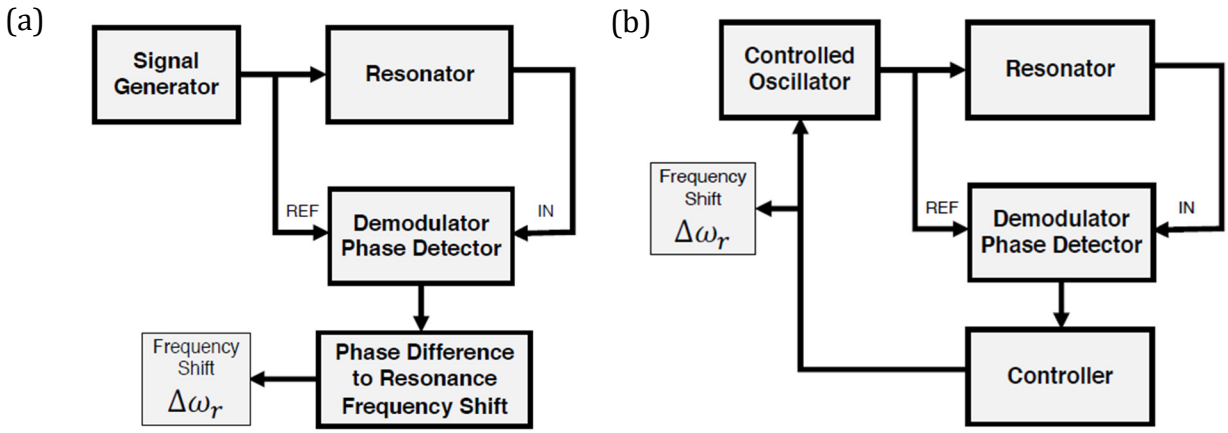

Figure 2.5. Block diagrams of (a) open loop experiment and (b) closed loop experiment.

Before expanding on the implications the use of a PLL has on noise, it is necessary to understand how a PLL operates. In a closed loop PLL, an oscillator produces a reference frequency signal, which enters the phase detector [16], [17], [29]. This is compared to the phase of the resonator to determine the error between the two signals as a voltage. Then the

error passes through a controller, which in the case of frequency locked nanomechanical resonator is a PI controller to reduce error propagation through the loop [16], [17]. The controller adjusts the signal of the controlled oscillator in a feedback loop. When there is a steady state error, the oscillator and resonator are at the same frequency and are therefore "locked".

Figure 2.6 shows a more detailed block diagram of a PLL in the phase domain and includes inputs due to thermomechanical noise (θ_{th}) and detection noise (θ_d). Starting at the top of the diagram in Figure 2.6, there is a frequency shift input of $\Delta\omega_e$, which is converted to a phase input through multiplication with the resonator time constant ($\tau_r = Q/2\omega_r$). Propagating through the loop, there is then an addition of resonator noise (θ_{th}). For the case considered in [16], this noise input is caused by thermomechanical noise. The signal then continues through $H_R(s)$, which is a transfer function that encapsulates the low pass filtering characteristics of the resonator being tested. Following $H_R(s)$, there is an additional noise input from detection noise (previously discussed in section 2.2.2). Continuing through the loop, there is then the comparison of the signal after propagating through the resonator to that from the controlled oscillator. This then passes through $H_L(s)$, which is a low pass filtering transfer function for the demodulator of the PLL. From here the signal passes through the proportional integral controller, H_{PI}, to correct for errors between the controlled oscillator and the resonator. The resulting output is a frequency shift, which is then converted back into a phase signal before propagating through the loop again.

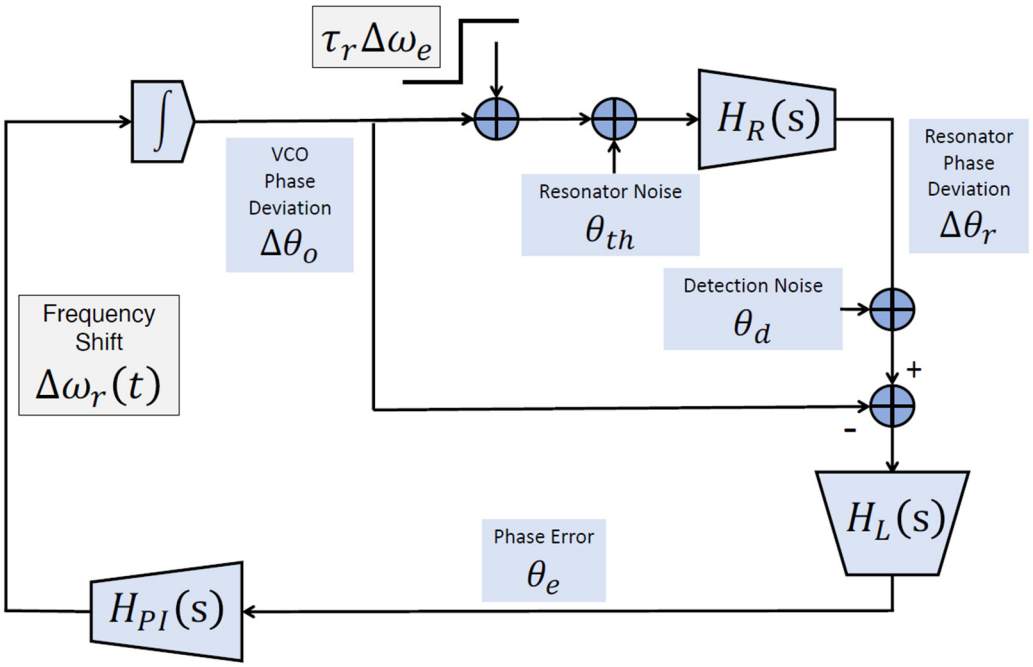

Figure 2.6. PLL model including contributions from thermomechanical noise and detection noise. Model is in the phase domain [16].

This model helps illustrate that resonator noise circulates through the frequency tracking scheme and can even increase the overall noise in the system if a high PLL bandwidth is implemented (see Figure 2.7). Mathematically, this can be expressed as a spectral density of fractional frequency fluctuations [16], [17]

$$S_y(\omega) = \frac{|H_{tmech}(j\omega)|^2 S_{y,tmech}(\omega) + |H_{det}(j\omega)|^2 S_{y,det}(\omega)}{\omega_r^2}, \tag{2.18}$$

where $H_{tmech}(j\omega)$ and $H_{det}(j\omega)$ are transfer functions that incorporate the PLL loop dynamics. The expression in Eq. (2.18) can be converted to an Allan deviation using Eq. (2.11).

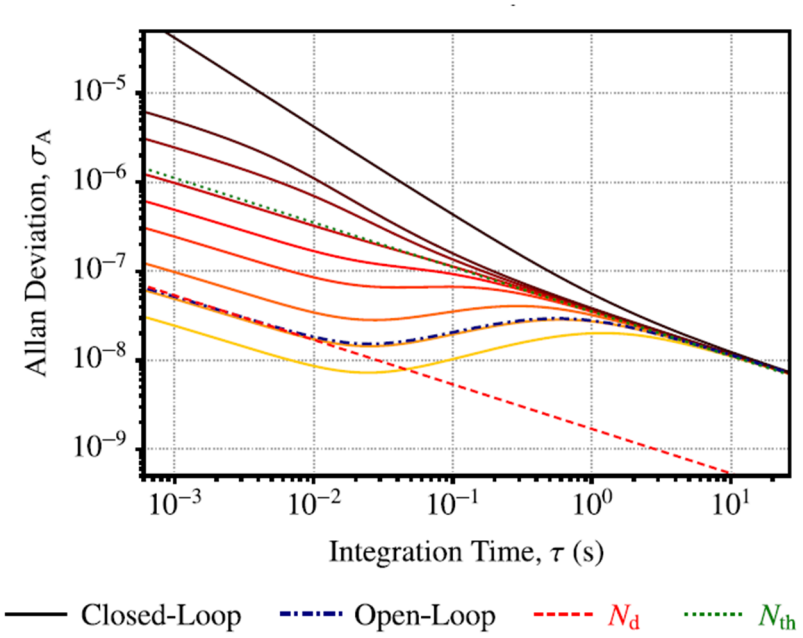

Figure 2.7. Effects of different PLL bandwidths. Increasing the PLL bandwidth results in an increase in the Allan deviation (BW values: 0.25 Hz, 0.5 Hz, 1 Hz, 2.5 Hz, 5 Hz, 10 Hz, 25 Hz, 50 Hz, 719.6 Hz).

3. Experimental Methods

The SiN drumhead resonators used in this research are fabricated using commercially available silicon wafers with ~100 nm thick low pressure chemical vapour deposition (LPCVD) low stress SiN. The wafers are patterned using photolithography and individual chips, with square membrane side-length sizes (L) between 1 mm – 12 mm, are then released by KOH etching. Post-fabrication, the thickness (d) of 12 different SiN films are measured using an ellipsometer (Horiba Ltd. UVISEL FUV-NIR), yielding thicknesses of 90 ± 1.7 nm. The actual membrane side lengths are then quantified by correcting for KOH over-etching. The over-etching magnitude is assessed, for every chip, by measuring relative change of the membrane frame dimension using a micrometer (Mitutoyo Inc.). An error of approximately 15 μm on the membrane size is estimated form the repeatability of this measurement.

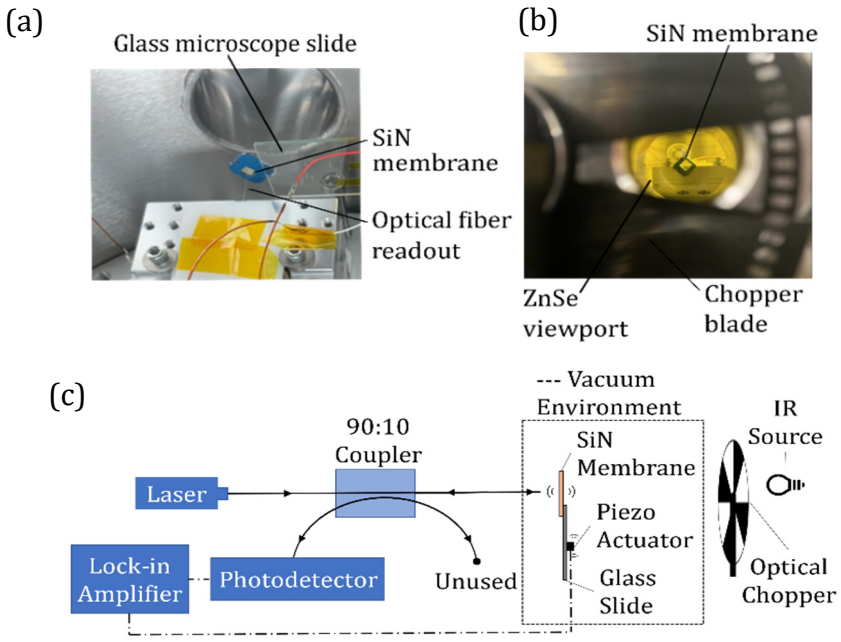

Figure 3.1. (a) SiN resonator mounted on a glass slide with a piezo actuator (not pictured). (b) View of SiN resonator from outside the vacuum chamber through the optical chopper and the ZnSe viewport. (c) Schematic of interferometer, resonator mounting, and IR source modulation.

Experiments are performed in a custom-made high vacuum testing chamber (~7.5×10^{-7} Torr). The corner of the resonator's silicon frame is mounted on a glass microscope slide

using Crystalbond™ shown in Figure 3.1 (a). Also attached to the glass slide is a shear piezo used to actuate the membrane. A fiber optic interferometer [30] records the resonator vibration amplitude and shifts in the resonance frequency. The interferometer is comprised of a 1550 nm Orion™ laser, a 90:10 optical fiber coupler, and an amplified photodetector (Thorlabs Inc. PDA20CS2) as seen in the schematic in Figure 3.1 (c). Signal from the photodetector is sampled using a Zurich Instrument Ltd. MFLI Lock-in amplifier. The lock-in amplifier is also used to actuate the shear piezo in a phase locked loop (PLL) that drives the membrane at its resonance frequency. Thermal infrared excitation of the membrane is performed with an infrared light source (ArcOptix S.A. ArcLight 1 – 25 μm IR source) located outside the vacuum chamber. The vacuum chamber is equipped with a zinc selenide (ZnSe) viewport from Thorlabs Inc. to allow transmission in the 600 nm - 16 μm spectral range (Fig 3.1b). Modulation of the IR source is performed using a Thorlabs Inc. optical chopper equipped with a 10% duty cycle blade.

4. Results

4.1 Heat Transport in SiN Drumhead Resonators

Two theoretical models were recently proposed for predicting thermal transport in drumhead resonators; both of these models can be applied to square drumhead resonators and include heat transfer by conduction and radiation [4], [11]. The model proposed in [4] uses a circular approximation with an effective radius ($r_{eff} = 1.252\ L/2$) to solve the heat equation in the square membrane. This model yields a characteristic thermal response time:

$$\tau_{th} = \frac{c_p \rho d}{8\sigma_{SB}\varepsilon T^3} x_{rad}, \tag{4.1}$$

where $c_p = 700 \frac{J}{kgK}$ [31] is the specific heat capacity, $\rho = 2900\ kg/m^3$ [32] is the material density, d is the membrane thickness, σ_{SB} is the Stefan-Boltzmann constant, ε is the total hemispherical emissivity of the membrane, and T is the ambient temperature. Also necessary for calculating the thermal time constant is the fraction ($x_{rad} = G_{rad}/G$) of the membrane radiative conductance (G_{rad}) over the total conductance (G, in units W/K). For a square membrane this is calculated as [4]

$$x_{rad} = 1 - \frac{2}{\beta r_{eff}} \frac{I_1(\beta r_{eff})}{I_0(\beta r_{eff})}, \tag{4.2}$$

where I_N is the Nth-order modified Bessel function of the first kind, and β is given by

$$\beta = \sqrt{\frac{8\sigma_{SB}\varepsilon T^3}{kd}}, \tag{4.3}$$

where k is the material conductivity of the membrane. In turn, the total conductance (G) between the membrane and its environment can be evaluated from x_{rad} and G_{rad}:

$$G = \frac{4\sigma_{SB}\varepsilon T^3 A}{x_{rad}}, \tag{4.4}$$

where $A = 2L^2$ for a suspended membrane exposed from both sides.

Conversely, the thermal response time model found in [11] solves for the square membrane temperature profile, and truncates the solution to the first-order Taylor expansion term:

$$\tau_{th} = \left(\frac{2\pi^2}{L^2}\frac{\sum_i d_i k_i}{\sum_i d_i \rho_i c_{p_i}} + \frac{8\sigma_{SB}\varepsilon T^3}{\sum_i d_i \rho_i c_{p_i}}\right)^{-1}, \tag{4.5}$$

where *i* indicates the layer number in the case of a multilayer assembly.

These models may be tested by exposing SiN membranes to IR radiation, which causes their temperature to increase, resulting in a measurable resonance frequency shift α, in Hz/K, given by [4]:

$$\alpha \approx -\frac{E\alpha_T}{2\sigma(1-\nu)} f_r \tag{4.6}$$

where α_T is the material coefficient of thermal expansion ($\sim 2.2 \times 10^{-6}$ K^{-1} for SiN), E is Young's modulus, $\sigma \approx 100$ MPa is the membrane's built-in tensile stress at room temperature, ν is the Poisson ratio, and f_r is the resonance frequency of the excited membrane eigenmode. Dividing this expression by G yields the responsivity to absorbed radiation, in Hz/W:

$$\Re_{abs} = \frac{\alpha}{G} H_{th}(j\omega), \tag{4.7}$$

where $H_{th}(j\omega)$ is a one pole low-pass filter that accounts for the thermal response time of the resonator:

$$H_{th}(j\omega) = \frac{1}{1 + j\omega\tau_{th}} \tag{4.8}$$

The responsivity to the incident radiation intensity, $\Re$, is finally given by multiplying $\Re_{abs}$ by the membrane absorption coefficient, which, according to Kirchhoff's law, equals membrane emissivity:

$$\Re = \varepsilon_{\lambda,\theta}(\lambda, 0)\Re_{abs}, \tag{4.9}$$

where $\varepsilon_{\lambda,\theta}(\lambda, 0)$ is the spectral normal emissivity. As shown in [4] and [14], for the case of a plain free-standing SiN membrane, the spectral normal emissivity $\varepsilon_{\lambda,\theta}(\lambda, 0)$ and the angle-integrated spectral hemispherical emissivity $\varepsilon_{\lambda}(\lambda)$ can be approximated as equal.

In order to benchmark models given in [4], [11], 90 ± 1.7 nm thick SiN membranes with side-lengths (L) between 1.5 mm – 12 mm are characterized. Once the internal oscillator of the lock-in is phase-locked to one of the membrane's eigenmodes, the membrane is intermittently exposed to our IR source at a rate of 4 Hz using the chopper system that blocks light for 90% of the cycle.

In Figure 4.1 (a), a resonance frequency shift of ~9 Hz is clearly resolved for resonance mode (3, 4), which is centered at around 76 kHz, for an $L = 6$ mm membrane. This would correspond to ~1.4 μW of absorbed radiation according to Eq. (7), in cases where $\omega << \frac{1}{\tau_{th}}$. In Figure 4.1 (b), a 0.006 Hz RMS residual frequency shift is obtained for mode (3, 4). This residual shift corresponds to a ~0.9 nW RMS sensor absorbed noise floor for a sensing bandwidth of 50 Hz, which is the lowest value achieved in this work.

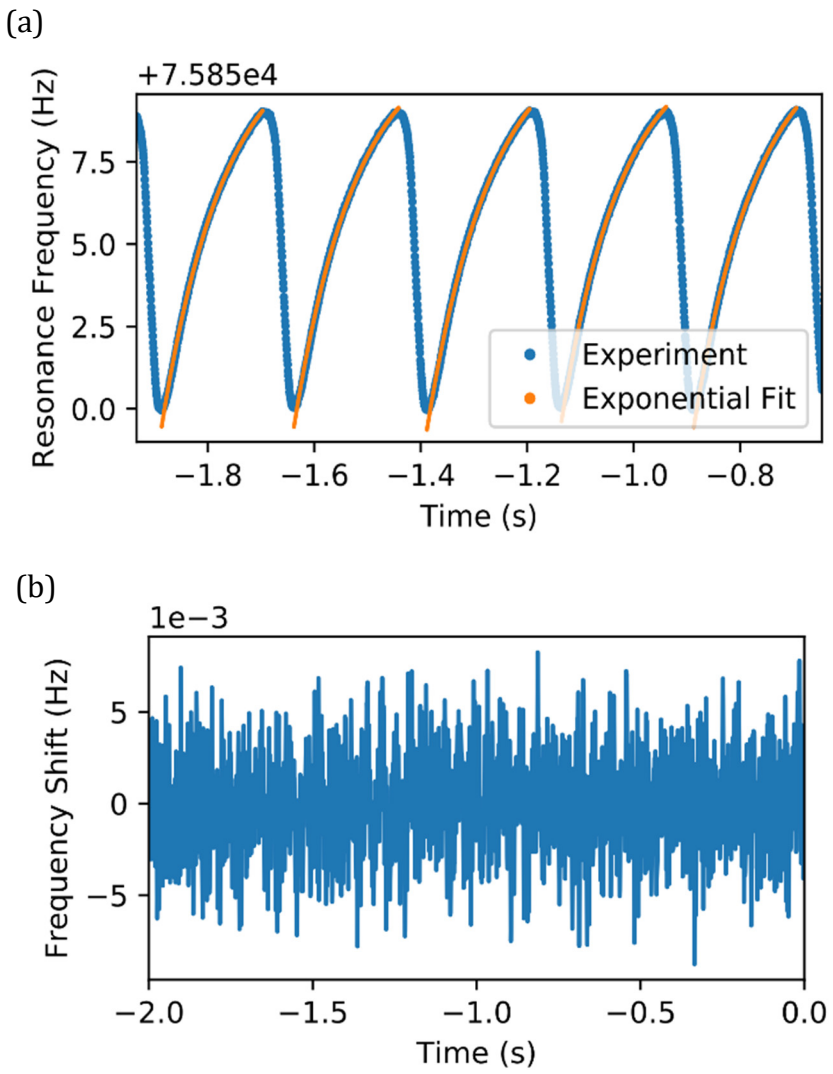

Figure 4.1. (a) Frequency response of mode (3, 4) of an L = 6 mm membrane as it is intermittently exposed to an IR source. When the membrane is exposed to the IR source, the SiN stress is reduced, resulting in a lower resonance frequency. (b) Frequency shift for mode (3, 4) of a 6 mm membrane when the membrane is not exposed to radiation. Frequency fluctuations equate to 0.006 Hz RMS noise.

Changes in resonance frequency over time are fit with exponential curves, as seen Figure 4.1 (a), to extract the characteristic thermal response time, τ_{th}, for multiple membrane dimensions. Accurate measurements of τ_{th} are ensured by configuring the PLL settings to a bandwidth fast enough for responding to thermally induced changes in the membrane resonance frequency. To determine these settings, the thermal time constant of various

membranes were measured with multiple PLL bandwidths. As can be seen in Figure 4.2 for the case of an $L = 6$ mm membrane, there are discrepancies in the value of the thermal time constant of the resonator at low PLL bandwidths. In this case, PLL bandwidths less than 20 Hz were too slow to accurately measure the resonator's thermal time constant, whereas a plateau region can be seen when PLL bandwidths are ≥ 20 Hz. Considering this effect, the PLL bandwidth for all measurements is set to $\geq$50 Hz, which was verified to be fast enough for all membrane sizes and eigenmodes used in this work. The demodulator bandwidth of the lock-in amplifier is set to five times the PLL bandwidth, i.e., to 250 Hz.

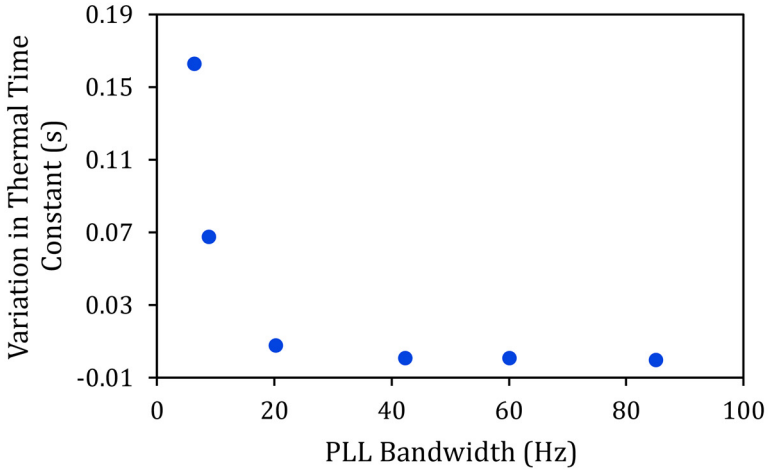

Figure 4.2. PLL calibration. Increasing the PLL bandwidth until the measured response time shows a plateau region, indicating that the PLL bandwidth is sufficiently fast to measure response time of the membrane. These measurements were performed for mode (2, 2) of a SiN membrane with a 6 mm side-length.

Thermal time constants measured for multiple membrane sizes with both theoretical models [4], [11] are shown in Figure 4.3 (a) and show relatively good correspondence with experimental values. The model curves are generated assuming hemispherical emissivity (ε) of the 90 ± 1.7 nm thick SiN membrane is 0.097 in accordance with the emissivity model proposed in [4] and later corrected in [14]. Furthermore, different conductivities (k) are used

when calculating the models to illustrate the effect of the large variability of values reported in literature [12], [13], [15]. The value of k reported in the most recent comparative study (2.7 W/mK [13]) yields the best correspondence with both heat transfer models, which further validates these recent conclusions [13]. It is therefore assumed $k = 2.7$ W/mK for the remainder of this work. In Figure 4.3 (b), experimental data for additional eigenmodes is presented and it can be seen that higher mode orders have slightly lower thermal time constant values when compared to mode (1, 1). This can be attributed to the mode shape; wherein higher order modes have antinodes that are closer to the heat-dissipating Si frame. In Figure 4.3 (b), both models [4], [11] predict relatively accurate thermal time constants for small membrane sizes (L); however, we note a systematic difference between the two existing models in the radiation dominated regions ($L \geq 6$ mm). It appears that keeping only the first-order Taylor term for the membrane temperature profile, as in [11], can lead to an overestimation of τ_{th} as it cannot properly model a fully radiation-dominated profile that is expected to have a box-like shape—i.e., constant temperature almost everywhere, and sharp changes in temperature near the membrane edges. We note however that the over estimation of is modest (~20%) and, in most practical case, it is likely to be within the error margin resulting from other factors such as uncertainties in material constants (e.g., ρ, c_p).

It should be emphasized that no fit parameters are used in Figure 4.3 (b) for matching measurement with theory curves. This indicates that the emissivity model for SiN proposed in [4] and [14], using the permittivity model given in [33], can likely be used with a high confidence level.

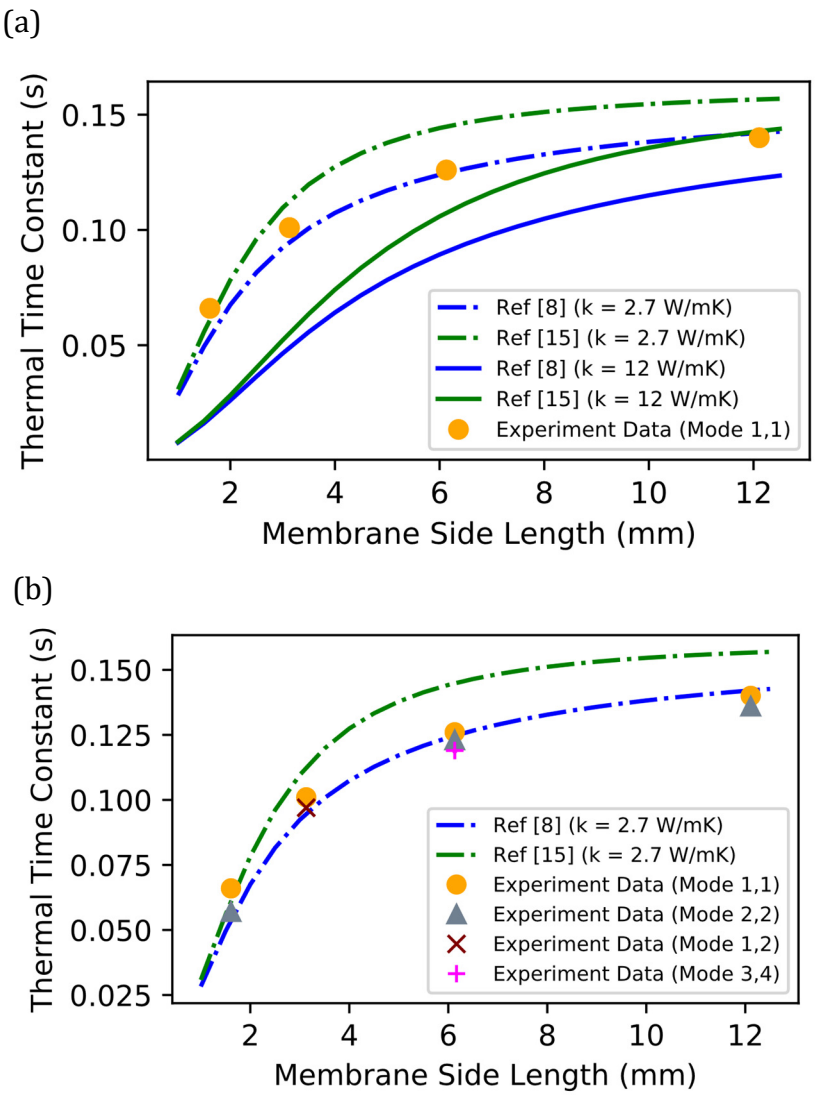

Figure 4.3. Characteristic thermal response time of SiN resonators. (a) Comparison of experimental thermal time constant data to the Circular approximation model [4] and first order Taylor expansion approximation [11] for SiN membranes with side-lengths ranging from 1.5 mm – 12 mm. The emissivity for both models is calculated using the analytical model from [4] while the value for thermal conductivity is varied to show the impact different reported literature values have on the models. (b) Additional vibration mode measurements compared with thermal time constant models from [4], [11] assuming the most recent literature value for thermal conductivity (k = 2.7 W/mK [13]) and ε = 0.097. A radiation dominant region can be seen for membrane side lengths ≳6 mm. For readability, only averaged measurements for multiple experimental trials are plotted on both figures. Error bars have been included to account for measurement repeatability, but the standard deviation values (on the order of 0.01 mm [x-axis] and 0.001 s [y-axis]) are too small to be visible.

4.2 Noise in Thermal Radiation Sensor

4.2.1 Noise Equivalent Power of Frequency Noise

Armed with an experimentally validated thermal transport model, expressions for frequency noise and for noise equivalent power (NEP) resulting from thermal fluctuation noise in frequency-shift based SiN radiation sensors can now be derived. The contribution of thermal fluctuation noise is also analyzed relative to other sources—namely thermomechanical noise and experimental detection noise—which have been more extensively discussed in previous work [16]–[18], [25].

Thermal fluctuation noise results from random energy exchanges between the resonator and its surrounding environment and therefore depends on the thermal conductance (G) of the structure. These exchanges affect the resonator temperature, which in turn results in resonance frequency shifts. The fractional frequency ($y = \frac{\Delta f}{f}$) fluctuation power density spectrum due thermal noise can be expressed by multiplying the temperature noise spectrum (S_{TT}, in K^2/Hz) [2], [19] by the normalized temperature sensitivity α/f_r:

$$S_{yy,th}(\omega) = S_{TT}(\omega)\frac{\alpha^2}{f_r^2} = \frac{4k_B T^2}{G}|H_{th}(j\omega)|^2\frac{\alpha^2}{f_r^2}\,, \tag{4.10}$$

where k_B is the Boltzmann constant. In turn, by combining this noise density function with the sensor responsivity [Eq. (4.9)], we can express the sensor noise equivalent power due to thermal fluctuation as:

$$NEP_{th} = \frac{\sqrt{S_{yy,th}}f_r}{|\Re|} = \frac{\sqrt{4k_B T^2 G}}{\varepsilon_{\lambda,\theta}(\lambda,0)}, \tag{4.11}$$

Eq. (4.10), combined with the expression of G given in Eq. (4.4), provides a closed-form expression for the fundamental NEP limit of drumhead resonators when used as thermal radiation sensors. Note that when calculating G for use in Eq. (4.11), the area A must account

for both sides of the membrane (i.e., $A = 2L^2$) unless surface functionalization allows for radiative coupling solely on the front surface. Care must also be given not to confuse spectral normal emissivity $\varepsilon_{\lambda,\theta}(\lambda, 0)$ with the total hemispherical emissivity ε, especially in cases, such as for SiN, where the former is strongly wavelength dependant [4], [14] (i.e., the gray body approximation does not apply).

Eq. (4.11) reduces to the classical fundamental detectivity limit of bolometers in the idealized case of a front-side coupled membrane ($A_{tot} = A_{front} = L^2$) with perfect absorption ($\varepsilon_{\lambda,\theta} = \varepsilon = 1$) and $x_{rad} = 1$ [1]:

$$D_{th}^{*} = \frac{\sqrt{A_{front}}}{NEP_{th}} = (16 k_B T^5 \sigma_{SB})^{-\frac{1}{2}}, \tag{4.12}$$

which is approximately $1.8 \times 10^{10} \frac{cm\sqrt{Hz}}{W}$ at $T = 300\ K$.

Obviously, other sources of noise must be accounted for in practical applications and thermomechanical noise is often the dominant one as indicated in [16]–[18], [25]. The spectral density of frequency noise induced by thermomechanical fluctuations is given by [16], [17]:

$$S_{yy,tmech}(\omega) = \frac{k_B T}{m_{eff} \omega_r^3 Q a_{rss}^2} |H_{tmech}(j\omega)|^2, \tag{4.13}$$

where Q is the quality factor of the resonator, m_{eff} is the effective resonator mass, ω_r is the angular resonance frequency, and a_{rss} is the amplitude of the resonator motion in steady state. $H_{tmech}(j\omega)$ denotes the resonator transfer function, which is a one-pole low pass filter similar to Eq. (4.8) but with a characteristic resonator time constant $\tau_{mech} = Q/(\pi f_r)$ instead of the thermal time constant (τ_{th}). Minimization of thermomechanical noise is usually achieved by using a driving amplitude at the onset of nonlinearity [26]:

$$a_{rss} = a_{crit} = 0.56 \frac{L}{\sqrt{Q}} \sqrt{\frac{\sigma}{E}}. \tag{4.14}$$

Using the same approach as for NEP_{th}, an expression for thermomechanical NEP can be derived using $S_{yy,tmech}$ in lieu of $S_{yy,th}$ in Eq. (4.11), and the expression for a_{rss} given in Eq. (4.14):

$$NEP_{tmech} = \frac{3.57\ G(1-\nu)}{\varepsilon_{\lambda,\theta}(\lambda,0)\ \alpha_T L}\sqrt{\frac{k_B T\sigma}{m_{eff}\omega_r^3 E}}\frac{|H_{tmech}(j\omega)|}{|H_{th}(j\omega)|}. \tag{4.15}$$

Another noise source that affects sensing performance is detection noise. This noise source encompasses contributions from the readout system, signal amplification, membrane transduction, and is therefore specific to each experiment. A convenient way of expressing detection noise is to quantify its magnitude relative to thermomechanical noise [16], [18]:

$$S_{yy,det}(\omega) = \kappa_d^2 \frac{k_B T}{m_{eff}\omega_r^3 Q a_{rss}^2}, \tag{4.16}$$

where κ_d is a dimensionless scaling parameter that indicates whether the background detection noise is sufficiently low for resolving thermomechanical displacement fluctuations (i.e., if $\kappa_d < 1$).

Within the prospect of realizing radiation sensors operating at the fundamental detectivity limit set by Eq. (5.3), it is insightful to evaluate the relative contribution of NEP_{th} relative NEP_{tmech}, which commonly dominates frequency noise in nanomechanical resonators [16]–[18], [25]. The relative contribution of NEP_{th} can be understood by defining the dimensionless ratio η:

$$\begin{aligned}\eta &= \frac{NEP_{th}(\omega)}{NEP_{tmech}(\omega)} = \left(\frac{S_{yy,th}}{S_{yy,tmech}}\right)^{1/2} \\ &= \frac{0.56\alpha_t L}{(1-\upsilon)}\sqrt{\frac{m_{eff}\omega_r^3 TE}{G\sigma}}\ \frac{|H_{th}(j\omega)|}{|H_{tmech}(j\omega)|}\ .\end{aligned} \tag{4.17}$$

By evaluating η (see Figure 4.4) for parameters of a typical large area membrane ($L = 6$ mm) used in this work, surprisingly it can be seen that thermal fluctuation noise can dominate

over thermomechanical noise (i.e., $\eta > 1$) in large area SiN membranes. This is in contrast with recent work on frequency noise in SiN string resonators, which clearly demonstrated thermomechanical fluctuation-dominated behaviour [18]. These current findings do not contradict this recent study [18], for which the ratio m_{eff}/G was much lower due to the string small size. Large portions of the study were also conducted for driving amplitudes smaller than a_{crit}, thus increasing the relative contribution of thermomechanical noise. In Figure 4.4, we also plot the actual predicted *NEP* values by considering $\varepsilon_{\lambda,\theta}(\lambda, 0) \approx 0.4$ to illustrate the performance of the membrane at $\lambda \approx 12$ µm, which is the maximum sensitivity wavelength of a SiN membrane [14]. We note that NEP_{th} ($\sim 4.1 \times 10^{-11}$ W/$\sqrt{Hz}$) dominates especially at frequencies greater than $\pi f_r/Q$ (vertical yellow dashed line), i.e., where the thermomechanical noise is filtered out by the system mechanical response time.

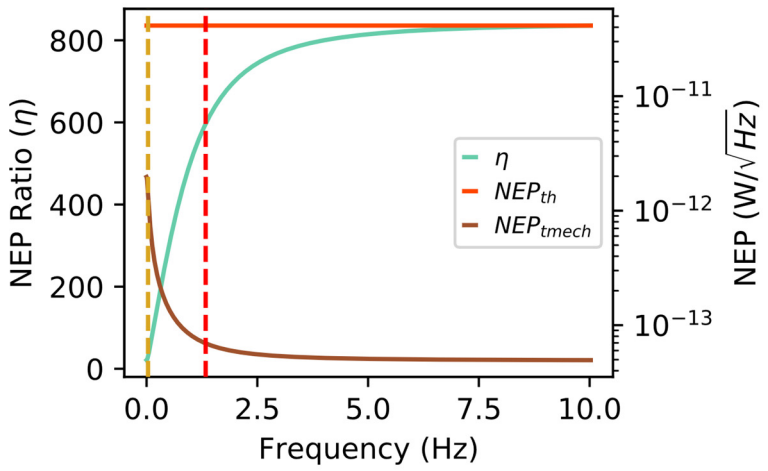

Figure 4.4. Ratio of thermal NEP to thermomechanical NEP. NEP for a typical membrane from this work (d = 90 nm, $L = 6\ mm, Q \approx 10^6, \sigma = 100\ MPa$), which is theoretically dominated by thermal noise. Membrane mode (3,4) ($f_r \approx 76\ kHz$) and critical amplitude actuation are considered in this case. The red dashed line represents the bandwidth imposed by the thermal time constant of the membrane ($1/2\pi\tau_{th}$) while the yellow dashed line represents the resonator mechanical bandwidth ($1/2\pi\tau_{mech}$).

Thermal fluctuation-dominated frequency noise, as demonstrated in Figure 4.4, is important as it could potentially enable thermal radiation sensors operating at the never

achieved fundamental detectivity limit set by Eq. (5.3). In principle, doing so would only require functionalizing the membrane front side to become a perfect radiation absorber (i.e., $\varepsilon_{\lambda,\theta} = \varepsilon = 1$) and to thermally isolate the backside (i.e., $\varepsilon_{\lambda,\theta} = \varepsilon = 0$), while not deteriorating the membrane mechanical properties.

In a practical situation, however, it is also imperative to consider noise after processing by the frequency tracking experimental apparatus (a PLL in our case). NEP values presented in Figure 4.4 only include intrinsic resonator noise and therefore exclude this contribution. As demonstrated in [16]–[18], PLL frequency tracking can increase noise by orders of magnitude, especially if the PLL bandwidth (50 Hz in the present example) is significantly greater than the resonator mechanical bandwidth ($1/2\pi\tau_{mech} \approx 0.03$ Hz in the present case). For this reason, accurately predicting experimental noise must account for loop dynamics by following the procedure outlined in [16], [17]. The experimentally measured frequency noise (6×10^{-3} Hz RMS, see Figure 4.1b) is good example, being ~3 orders of magnitude greater than the frequency noise predicted by Eq. (4.10), (4.13) if simply integrating these expressions over the 50 Hz PLL bandwidth. Doing so underestimates noise in the system by predicting values on the order of $\sim 10^{-6}$ Hz RMS. In contrast, considering the complete PLL loop dynamics along with detection and thermomechanical noise (see section 4.2.2) gives a better estimation of experimentally measured noise.

4.2.2 Allan Deviation of Frequency Noise

The measured experimental noise in Figure 4.1 (b), is higher than predicted by the equations for the intrinsic resonator noise (Eq. 4.11, 4.15) due to the use of a PLL frequency tracking scheme. Such behaviour is expected and predictable using the theory given in [16], [17], and is especially pronounced for PLL bandwidths that are higher than the resonator bandwidth [$BW = (\pi f_r)/Q$]. High PLL bandwidths (~50 Hz) are required in the present experiment for accurately characterizing the SiN membrane thermal response time (see

Figure 4.2). Incorporating PLL loop dynamics into the noise analysis performed above is possible by computing the predicted Allan Deviation due to thermomechanical and detection noise as given in [16]–[18]:

$$\sigma_y(\tau) = \frac{2}{\sqrt{\pi}\tau}\left[\int_{-\infty}^{+\infty} \frac{\left[\sin\left(\frac{\omega\tau}{2}\right)\right]^4}{\omega^2} S_y(\omega)\, d\omega\right]^{\frac{1}{2}}, \tag{4.18}$$

where τ is the integration time and $S_y(\omega)$ is the spectral density of the fractional frequency fluctuations. Using Eq. (4.13) and (4.16) from the above section, the frequency noise from thermomechanical and detection noise is

$$S_y(\omega) = \frac{k_B T}{m_{eff}\omega_r^3 Q a_{rss}^2} |H_{tmech}^{PLL}(j\omega)|^2 + \kappa_d^2 \frac{k_B T}{m_{eff}\omega_r^3 Q a_{rss}^2} |H_{det}^{PLL}(j\omega)|^2, \tag{4.19}$$

where H_{tmech}^{PLL} and H_{det}^{PLL} are transfer functions for thermomechanical noise and detection noise in a closed-loop system [16], [17]:

$$H_{tmech}^{PLL}(s) = \frac{\left(sK_p + K_i\right)H_L(s)}{s^2 + \frac{s}{\tau_{mech}} + \left(sK_p + K_i\right)H_L(s)}, \tag{4.20}$$

$$H_{det}^{PLL}(s) = \frac{1}{H_{tmech}(s)} \frac{\left(sK_p + K_i\right)H_L(s)}{s^2 + \frac{s}{\tau_{mech}} + \left(sK_p + K_i\right)H_L(s)}. \tag{4.21}$$

In the above expressions, two transfer functions are applied: the resonator filter $H_{tmech}(s) = \frac{1}{1+s\tau_{mech}}$ and the demodulator filter $H_L(s) = \frac{1}{1+s\tau_{demod}}$. Also introduced are the loop controller parameters K_p (proportional) and K_i (integral), which are calculated as a function of the PLL bandwidth [16], [17]:

$$K_p = \omega_{PLL}\,, \qquad K_i = \frac{\omega_{PLL}}{\tau_{mech}} \tag{4.22}$$

Note that Eq 4.18 – 4.21 do not include thermal fluctuation-induced frequency noise $S_{yy,th}(\omega)$ because a transfer function $H_{th}^{PLL}(s)$ for this noise term is unknown at this time. Deriving such term would be the logical next step to this work.

In Figure 4.5 (a) a 5-minute frequency noise measurement is shown (similar to Figure 4.1 b of the main text, but for a longer acquisition time), which is then converted to an Allan deviation and plotted with the model detailed in the equations above (Figure 4.5 b). In Figure 4.5 (b), the experiment data is compared with the Allan deviation for a 0.03 Hz PLL bandwidth, which is equivalent to the mechanical bandwidth of the resonator, and for a 50 Hz PLL bandwidth, which was the bandwidth used in the experiments to resolve the thermal response time. Here it can clearly be seen that there is an increase in system noise by ~3 orders of magnitude for a 50 Hz PLL bandwidth, compared with the noise that would be expected if the PLL bandwidth had been matched to the resonator bandwidth. In the latter case, the Allan deviation closely follows the asymptotic behaviours for thermomechanical and detection noise (i.e., no extra noise is expected above the predictions of Eq. 4.13, 4.16). The noise present in the experiment more closely corresponds to the theoretical model for the 50 Hz PLL bandwidth. This further supports the case that the higher noise levels seen experimentally are due to the use of a high PLL bandwidth. At $\tau \approx 0.03$ s, there is an increase in the experimental Allan deviation, which is not present in the model. The exact source of this increase is still unknown; however, a possible cause could be noise introduced while driving our membrane near the onset of nonlinearity. As is commonly seen experimentally [18], noise due to drift dominates the membrane at higher integration times resulting in further deviation from the theoretical model.

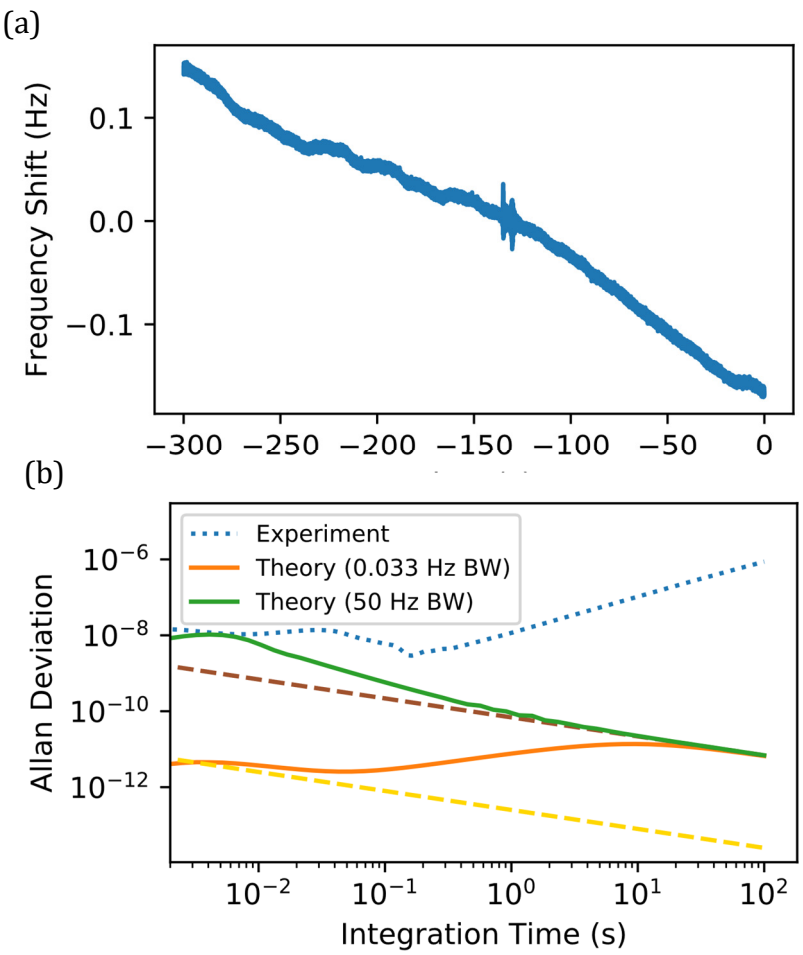

Figure 4.5. (a) Frequency noise trace over a duration of 5-minutes for mode (3, 4) of an $L = 6$ mm membrane. (b) Theoretical thermomechanical/detection Allan Deviations (solid lines) and experimental (dotted line) Allan deviations of mode (3,4) of an $L = 6$ mm membrane. Increasing the PLL bandwidth from 0.03 Hz to 50 Hz results in an increase in the Allan deviation by ~3 orders of magnitude. For a PLL bandwidth equivalent to the resonator bandwidth (0.03 Hz) the Allan deviation follows the detection noise asymptote (yellow dashed line) and the thermomechanical noise asymptote (brown dashed line)

To calculate the detection noise ($S_{yy,det}$, Eq. 4.16) in the setup and generate the plot seen in Figure 4.5 (b), the dimensionless parameter κ_d is measured, which indicates the relative contributions of thermomechanical and detection noise. This parameter was determined experimentally by measuring the power spectral density (PSD) over 100 Hz bandwidth near the resonance peak of the membrane when no drive was provided by the shear piezo in the

setup. Under these conditions there is still see a peak in the PSD at the resonance frequency of the resonator due to thermomechanical noise. Taking the ratio between the $\sqrt{PSD}$ of the background detection noise (red dashed line in Figure 4.6) and the $\sqrt{PSD}$ of the resonance peak induced by thermomechanical noise (green dashed line in Figure 4.6) results in a κ_d value of 0.006.

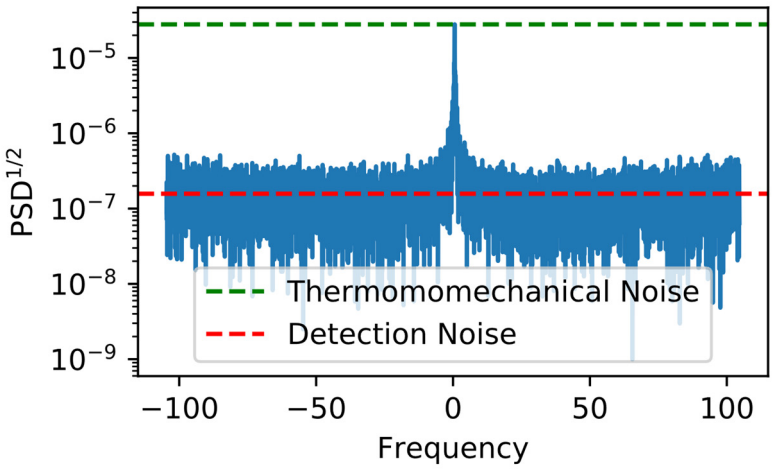

Figure 4.6. Measurement of κ_d. Spectrum over 100 Hz BW near the resonance peak of the membrane is measured when no actuation is provided by the shear piezo (i.e., resonator motion is a result of random motion of particles around and within the membrane). The $\sqrt{PSD}$ ratio between the background detection noise (red dashed line) and the resonance peak caused by thermomechanical noise (green dashed line) yields κ_d = 0.006.

5. Conclusion

In the first portion of this work, after comparing two recently proposed models for the thermal response time in SiN resonators [4], [11], we find that they both correspond relatively well with experimental results at small membrane sizes (i.e. non-radiation dominant resonators). When using the most recent value for thermal conductivity [13] and the analytical emissivity model from [4], [14] we see that the circular approximation model for calculating the thermal time constant more closely corresponds with the experimental data presented than the Taylor approximation model for membrane sizes ≥ 6. However, difference between the two models is modest and would likely be acceptable for most applications.

Secondly, using our experimentally validated heat transport model, we show that thermal fluctuation noise can often dominate intrinsic frequency noise in both large and small area membranes. However, experimentally verifying this is currently not possible due to the unknown effect of our PLL frequency tracking scheme on thermal fluctuation noise. While thermomechanical and detection noise have been analyzed in the context of PLL frequency tracking [16]–[18], the same analysis currently does not exist for thermal fluctuation noise. Performing this analysis is the logical next step to our work. Ultimately, a complete understanding thermal fluctuation induced frequency noise could lead to the design of radiation sensors achieving the fundamental detectivity limit of bolometric thermal radiation sensors experimentally.

References

[1] A. Rogalski, “Infrared detectors: status and trends,” *Progress in Quantum Electronics*, vol. 27, no. 2, pp. 59–210, Jan. 2003, doi: 10.1016/S0079-6727(02)00024-1.

[2] L. Laurent, J.-J. Yon, J.-S. Moulet, M. Roukes, and L. Duraffourg, “12 – μ m-Pitch Electromechanical Resonator for Thermal Sensing,” *Phys. Rev. Applied*, vol. 9, no. 2, p. 024016, Feb. 2018, doi: 10.1103/PhysRevApplied.9.024016.

[3] M. Piller, N. Luhmann, M.-H. Chien, and S. Schmid, “Nanoelectromechanical infrared detector,” in *Optical Sensing, Imaging, and Photon Counting: From X-Rays to THz 2019*, Sep. 2019, vol. 11088, p. 1108802. doi: 10.1117/12.2528416.

[4] C. Zhang, M. Giroux, T. A. Nour, and R. St-Gelais, “Radiative Heat Transfer in Freestanding Silicon Nitride Membranes,” *Phys. Rev. Applied*, vol. 14, no. 2, p. 024072, Aug. 2020, doi: 10.1103/PhysRevApplied.14.024072.

[5] X. C. Zhang, E. B. Myers, J. E. Sader, and M. L. Roukes, “Nanomechanical Torsional Resonators for Frequency-Shift Infrared Thermal Sensing,” *Nano Lett.*, vol. 13, no. 4, pp. 1528–1534, Apr. 2013, doi: 10.1021/nl304687p.

[6] N. Snell, C. Zhang, G. Mu, and R. St-Gelais, “Nanowatt Thermal Radiation Sensing using Silicon Nitride Nanomechanical Resonators,” in *2020 Photonics North (PN)*, May 2020, pp. 1–1. doi: 10.1109/PN50013.2020.9167002.

[7] M. Giroux, C. Zhang, N. Snell, G. Mu, M. Stephan, and R. St-Gelais, “High Resolution Measurement of Near-Field Radiative Heat Transfer enabled by Nanomechanical Resonators,” Jun. 2021, Accessed: Jul. 06, 2021. [Online]. Available: https://arxiv.org/abs/2106.09504v1

[8] L. Vicarelli, A. Tredicucci, and A. Pitanti, "Micromechanical bolometers for sub-Terahertz detection at room temperature," *arXiv:2107.12170 [physics]*, Jul. 2021, Accessed: Aug. 06, 2021. [Online]. Available: http://arxiv.org/abs/2107.12170

[9] B. M. Zwickl *et al.*, "High quality mechanical and optical properties of commercial silicon nitride membranes," *Appl. Phys. Lett.*, vol. 92, no. 10, p. 103125, Mar. 2008, doi: 10.1063/1.2884191.

[10] R. St-Gelais, S. Bernard, C. Reinhardt, and J. C. Sankey, "Swept-Frequency Drumhead Optomechanical Resonators," *ACS Photonics*, vol. 6, no. 2, pp. 525–530, Feb. 2019, doi: 10.1021/acsphotonics.8b01519.

[11] M. Piller *et al.*, "Thermal radiation dominated heat transfer in nanomechanical silicon nitride drum resonators," *Appl. Phys. Lett.*, vol. 117, no. 3, p. 034101, Jul. 2020, doi: 10.1063/5.0015166.

[12] A. Sikora *et al.*, "Highly sensitive thermal conductivity measurements of suspended membranes (SiN and diamond) using a 3ω-Völklein method," *Review of Scientific Instruments*, vol. 83, no. 5, p. 054902, May 2012, doi: 10.1063/1.4704086.

[13] H. Ftouni *et al.*, "Thermal conductivity of silicon nitride membranes is not sensitive to stress," *Phys. Rev. B*, vol. 92, no. 12, p. 125439, Sep. 2015, doi: 10.1103/PhysRevB.92.125439.

[14] C. Zhang, A. Bouchard, M. Giroux, T. A. Nour, and R. St-Gelais, "Erratum: Radiative Heat Transfer in Freestanding Silicon Nitride Membranes [Phys. Rev. Appl. 14, 024072 (2020)]," *Phys. Rev. Applied*, vol. 16, no. 1, p. 019901, Jul. 2021, doi: 10.1103/PhysRevApplied.16.019901.

[15] X. Zhang and C. P. Grigoropoulos, “Thermal conductivity and diffusivity of free-standing silicon nitride thin films,” *Review of Scientific Instruments*, vol. 66, no. 2, pp. 1115–1120, Feb. 1995, doi: 10.1063/1.1145989.

[16] A. Demir, “Understanding fundamental trade-offs in nanomechanical resonant sensors,” *Journal of Applied Physics*, vol. 129, no. 4, p. 044503, Jan. 2021, doi: 10.1063/5.0035254.

[17] A. Demir and M. S. Hanay, “Fundamental Sensitivity Limitations of Nanomechanical Resonant Sensors Due to Thermomechanical Noise,” *IEEE Sensors Journal*, vol. 20, no. 4, pp. 1947–1961, Feb. 2020, doi: 10.1109/JSEN.2019.2948681.

[18] P. Sadeghi, A. Demir, L. G. Villanueva, H. Kähler, and S. Schmid, “Frequency fluctuations in nanomechanical silicon nitride string resonators,” *Phys. Rev. B*, vol. 102, no. 21, p. 214106, Dec. 2020, doi: 10.1103/PhysRevB.102.214106.

[19] J. R. Vig and Yoonkee Kim, “Noise in microelectromechanical system resonators,” *IEEE Transactions on Ultrasonics, Ferroelectrics, and Frequency Control*, vol. 46, no. 6, pp. 1558–1565, Nov. 1999, doi: 10.1109/58.808881.

[20] A. N. Cleland and M. L. Roukes, “Noise processes in nanomechanical resonators,” *Journal of Applied Physics*, vol. 92, no. 5, pp. 2758–2769, Aug. 2002, doi: 10.1063/1.1499745.

[21] W. Riley and D. A. Howe, “Handbook of Frequency Stability Analysis,” Jul. 2008, Accessed: Sep. 03, 2021. [Online]. Available: https://www.nist.gov/publications/handbook-frequency-stability-analysis

[22] D. W. Allan, “Statistics of atomic frequency standards,” *Proceedings of the IEEE*, vol. 54, no. 2, pp. 221–230, Feb. 1966, doi: 10.1109/PROC.1966.4634.

[23] D. W. Allan, “Time and Frequency (Time-Domain) Characterization, Estimation, and Prediction of Precision Clocks and Oscillators,” *IEEE Trans. Ultrason., Ferroelect., Freq. Contr.*, vol. 34, no. 6, pp. 647–654, Nov. 1987, doi: 10.1109/T-UFFC.1987.26997.

[24] M. Piller, J. Hiesberger, E. Wistrela, P. Martini, N. Luhmann, and S. Schmid, “Thermal IR detection with nanoelectromechanical silicon nitride trampoline resonators,” May 2021, Accessed: Jun. 28, 2021. [Online]. Available: https://arxiv.org/abs/2105.03999v1

[25] M. Sansa *et al.*, “Frequency fluctuations in silicon nanoresonators,” *Nature Nanotechnology*, vol. 11, no. 6, pp. 552–558, Jun. 2016, doi: 10.1038/nnano.2016.19.

[26] S. Schmid, L. G. Villanueva, and M. L. Roukes, *Fundamentals of Nanomechanical Resonators*. Springer International Publishing, 2016. doi: 10.1007/978-3-319-28691-4.

[27] C. Di Natale, C. Giampaolo, and A. D’Amico, “Study of the noise in adsorption–desorption phenomena using the Allan variance and a quartz microbalance,” *Sensors and Actuators B: Chemical*, vol. 65, no. 1, pp. 227–231, Jun. 2000, doi: 10.1016/S0925-4005(99)00294-4.

[28] Y. T. Yang, C. Callegari, X. L. Feng, and M. L. Roukes, “Surface Adsorbate Fluctuations and Noise in Nanoelectromechanical Systems,” *Nano Lett*, vol. 11, no. 4, Apr. 2011, doi: 10.1021/nl2003158.

[29] G.-C. Hsieh and J. C. Hung, “Phase-locked loop techniques. A survey,” *IEEE Transactions on Industrial Electronics*, vol. 43, no. 6, pp. 609–615, Dec. 1996, doi: 10.1109/41.544547.

[30] D. Rugar, H. J. Mamin, and P. Guethner, “Improved fiber-optic interferometer for atomic force microscopy,” *Appl. Phys. Lett.*, vol. 55, no. 25, pp. 2588–2590, Dec. 1989, doi: 10.1063/1.101987.

[31] C. H. Mastrangelo, Y.-C. Tai, and R. S. Muller, “Thermophysical properties of low-residual stress, Silicon-rich, LPCVD silicon nitride films,” *Sensors and Actuators A: Physical*, vol. 23, no. 1, pp. 856–860, Apr. 1990, doi: 10.1016/0924-4247(90)87046-L.

[32] G. Carlotti *et al.*, “Measurement of the elastic and viscoelastic properties of dielectric films used in microelectronics,” *Thin Solid Films*, vol. 414, no. 1, pp. 99–104, Jul. 2002, doi: 10.1016/S0040-6090(02)00430-3.

[33] “Dielectric Constant & Relative Permittivity » Electronics Notes.” https://www.electronics-notes.com/articles/basic_concepts/capacitance/dielectric-constant-relative-permittivity.php (accessed Oct. 19, 2020).

[34] H. Zhang and E. S. Kim, “Micromachined acoustic resonant mass sensor,” *Journal of Microelectromechanical Systems*, vol. 14, no. 4, pp. 699–706, Aug. 2005, doi: 10.1109/JMEMS.2005.845405.

[35] M. S. Hanay *et al.*, “Single-protein nanomechanical mass spectrometry in real time,” *Nature Nanotechnology*, vol. 7, no. 9, Art. no. 9, Sep. 2012, doi: 10.1038/nnano.2012.119.

[36] J. Chaste, A. Eichler, J. Moser, G. Ceballos, R. Rurali, and A. Bachtold, “A nanomechanical mass sensor with yoctogram resolution,” *Nature Nanotechnology*, vol. 7, no. 5, Art. no. 5, May 2012, doi: 10.1038/nnano.2012.42.

[37] J. Moser *et al.*, “Ultrasensitive force detection with a nanotube mechanical resonator,” *Nature Nanotechnology*, vol. 8, no. 7, Art. no. 7, Jul. 2013, doi: 10.1038/nnano.2013.97.

[38] D. Hälg *et al.*, “Membrane-Based Scanning Force Microscopy,” *Phys. Rev. Applied*, vol. 15, no. 2, p. L021001, Feb. 2021, doi: 10.1103/PhysRevApplied.15.L021001.

6. Appendix 1 – Submitted Article Original Version

Nikaya Snell, Chang Zhang, Gengyang Mu, Alexandre Bouchard, Raphael St-Gelais
Department of Mechanical Engineering, University of Ottawa, Ottawa, ON, Canada

6.1 Abstract

Silicon nitride (SiN) drumhead resonators offer a promising platform for thermal sensing due to their high mechanical quality factor and the high temperature sensitivity of their resonance frequency. As such, gaining an understanding of heat transport in SiN resonators as well as their sensing noise limitations is of interest, both of which are goals of the present work. We first present new experimental results on radiative heat transport in SiN membrane, which we use for benchmarking two recently proposed theoretical models. We measure the characteristic thermal response time of square SiN membranes with a thickness of 90 ± 1.7 nm and side lengths from 1.5 to 12 mm. A clear transition between radiation and conduction dominated heat transport is measured, in close correspondence with theory. In the second portion of this work, we use our experimentally validated heat transport model to provide a closed-form expression for thermal fluctuation-induced frequency noise in SiN membrane resonators. We find that, for large area SiN membranes, thermal fluctuations can be greater than thermomechanical contributions to frequency noise. For the specific case of thermal radiation sensing applications, we also derive the noise equivalent power resulting from thermal fluctuation-induced frequency noise, and we show in which conditions it reduces to the classical detectivity limit of thermal radiation sensors. Our work therefore provides a path towards achieving thermal radiation sensors operating at the never attained fundamental detectivity limit of bolometric sensing. We also identify questions that remain

when attempting to push the limits of radiation sensing, in particular, the effect of thermal fluctuation noise in closed-loop frequency tracking schemes remain to be clarified.

6.2 Introduction

A variety of sensing technologies have been built using nanomechanical resonators, such as mass [34]–[36], force [37], [38], and thermal radiation sensors [2]–[8]. The use of silicon nitride (SiN) resonators in thermal sensing schemes is especially appealing due to the ability to form high quality factor resonators whose resonance frequency is highly sensitive to temperature changes [3], [4], [9]–[11]. To further the development of SiN thermal sensors, there has been recent interest in understanding the radiative and conductive heat transport in SiN membranes [4], [11]–[13] .

Recent studies [4], [11], including one by the authors of the current work [4], proposed models for thermal radiation heat transport in square silicon nitride membranes using either a circular approximation [4] or a first-order Taylor expansion approximation [11]. A distinctive feature of our work [4] was the inclusion an analytical model for the emissivity of SiN. On the other hand, experimental validation of our model was only preliminary. A single membrane size was tested experimentally using a continuous-wave IR radiator, whose static nature resulted in relatively large uncertainties due to drift. In [11], a first order Taylor model corresponded well with experimental measurements for 50 nm thick square membranes. Dynamic measurements were performed for various membranes side-lengths up to 4 mm, for which the fraction of heat transfer occurring by radiation (x_{rad}) is predicted to be approximately 70% [4], i.e., where 30% of the total heat transfer still occurs via conduction. Despite this conclusive demonstration, observation of a fully radiation-dominated region is still desirable. This would notably allow a more direct confirmation of existing models [4], [14] and measurements [11] on the emissivity of SiN, without the need to account for conduction heat transfer.

The goal of this work is two-fold. We first provide additional experimental validation for these models by performing dynamic measurements of the thermal response time of SiN membranes for membrane sizes up to 12 mm. We observe a clear region of radiation-dominated heat transport ($x_{rad} \approx 90\%$) that allows for a detailed comparison with recently proposed models for thermal transport [4], [11], emissivity [4], [14], and thermal conductivity [12], [13], [15].

Secondly, we use our validated model for heat transport to derive a closed-form expression for thermal fluctuation-induced frequency noise in drum resonator-based radiation sensors. We show that thermal fluctuation noise can potentially dominate over thermomechanical frequency noise in large area SiN. This outlines the importance of considering thermal fluctuation noise together with other noise sources (i.e., thermomechanical and detection noise) within recently proposed frameworks for frequency noise in nanomechanical resonators [16]–[20].

6.3 Experimental Methods

The SiN drumhead resonators used in this research are fabricated using commercially available silicon wafers with ~ 100 nm thick low pressure chemical vapour deposition (LPCVD) low stress SiN. The wafers are patterned using photolithography and individual chips, with square membrane side-length sizes (L) between 1 mm – 12 mm, are then released by KOH etching. Post-fabrication, the thickness (d) of 12 different SiN films are measured using an ellipsometer (Horiba Ltd. UVISEL FUV-NIR), yielding thicknesses of 90 ± 1.7 nm. The actual membrane side lengths are then quantified by correcting for KOH over-etching. The over-etching magnitude is assessed, for every chip, by measuring relative change of the membrane frame dimension using a micrometer (Mitutoyo Inc.). A membrane size error of approximately 15 μm is estimated from the repeatability of this measurement.

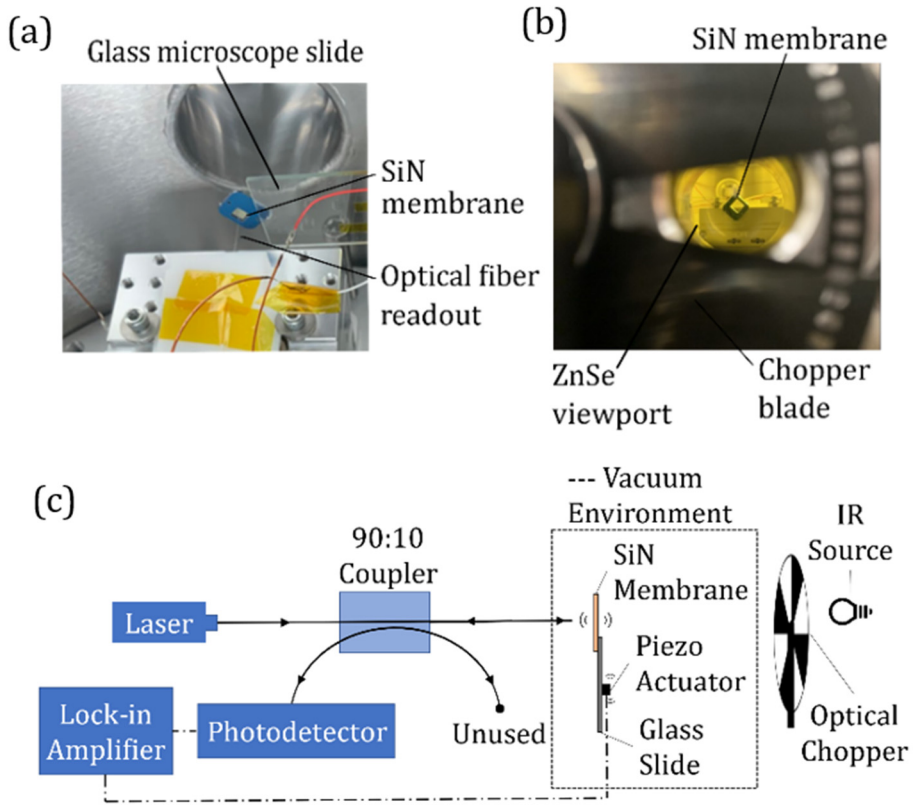

FIG. 1. (a) SiN resonator mounted on a glass slide with a piezo actuator (not pictured). (b) View of SiN resonator from outside the vacuum chamber through the optical chopper and the ZnSe viewport. (c) Schematic of interferometer, resonator mounting, and IR source modulation.

Experiments are performed in a custom-made high vacuum testing chamber ($\sim 7.5 \times 10^{-7}$ Torr). The corner of the resonator's silicon frame is mounted on a glass microscope slide using Crystalbond™ shown in Fig 1 (a). Also attached to the glass slide is a shear piezo used to actuate the membrane. A fiber optic interferometer [30] records the resonator vibration amplitude and shifts in the resonance frequency. The interferometer is comprised of a 1550 nm Orion™ laser, a 90:10 optical fiber coupler, and an amplified photodetector (Thorlabs Inc. PDA20CS2) as seen in the schematic in Fig. 1 (c). Signal from the photodetector is sampled using a Zurich Instrument Ltd. MFLI Lock-in amplifier. The lock-in amplifier is also used to actuate the shear piezo in a phase locked loop (PLL) that drives the membrane at its resonance frequency. Thermal infrared excitation of the membrane is performed with an

infrared light source (ArcOptix S.A. ArcLight 1 – 25 μm IR source) located outside the vacuum chamber. The vacuum chamber is equipped with a zinc selenide (ZnSe) viewport from Thorlabs Inc. to allow transmission in the 600 nm - 16 μm spectral range. Modulation of the IR source is performed using a Thorlabs Inc. optical chopper equipped with a 10% duty cycle blade.

6.4 Heat Transport in SiN Drum Resonators

Two theoretical models were recently proposed for predicting thermal transport in drumhead resonators; both of these models can be applied to square drumhead resonators and include heat transfer by conduction and radiation [4], [11]. The model proposed in [4] uses a circular approximation with an effective radius ($r_{eff} = 1.252\ L/2$) to solve the heat equation in the square membrane. This model yields a characteristic thermal response time:

$$\tau_{th} = \frac{c_p \rho d}{8\sigma_{SB}\varepsilon T^3} x_{rad}, \tag{1}$$

where $c_p = 700 \frac{J}{kgK}$ [31] is the specific heat capacity, $\rho = 2900\ kg/m^3$ [32] is the material density, d is the membrane thickness, σ_{SB} is the Stefan-Boltzmann constant, ε is the total hemispherical emissivity of the membrane, and T is the ambient temperature. Also necessary for calculating the thermal time constant is the fraction ($x_{rad} = G_{rad}/G$) of the membrane radiative conductance (G_{rad}) over the total conductance (G, in units W/K). For a square membrane this is calculated as [4]

$$x_{rad} = 1 - \frac{2}{\beta r_{eff}} \frac{I_1(\beta r_{eff})}{I_0(\beta r_{eff})}, \tag{2}$$

where I_N is the Nth-order modified Bessel function of the first kind, and β is given by

$$\beta = \sqrt{\frac{8\sigma_{SB}\varepsilon T^3}{kd}}, \tag{3}$$

where k is the material conductivity of the membrane. In turn, the total conductance (G) between the membrane and its environment can be evaluated from x_{rad} and G_{rad}:

$$G = \frac{4\sigma_{SB}\varepsilon T^3 A}{x_{rad}}, \tag{4}$$

where $A = 2L^2$ for a suspended membrane exposed from both sides.

Conversely, the thermal response time model found in [11] solves for the square membrane temperature profile, and truncates the solution to the first-order Taylor expansion term:

$$\tau_{th} = \left(\frac{2\pi^2}{L^2}\frac{\sum_i d_i k_i}{\sum_i d_i \rho_i c_{p_i}} + \frac{8\sigma_{SB}\varepsilon T^3}{\sum_i d_i \rho_i c_{p_i}}\right)^{-1}, \tag{5}$$

where *i* indicates the layer number in the case of a multilayer assembly.

These models are compared to experiments by exposing SiN membranes to IR radiation, which causes their temperature to increase, resulting in a measurable resonance frequency shift α, in Hz/K, given by [4]:

$$\alpha \approx -\frac{E\alpha_T}{2\sigma(1-\nu)} f_r \tag{6}$$

where α_T is the material coefficient of thermal expansion ($\sim 2.2 \times 10^{-6}$ K^{-1} for SiN), E is Young's modulus, $\sigma \approx 100$ MPa is the membrane's built-in tensile stress at room temperature, ν is the Poisson ratio, and f_r is the resonance frequency of the excited membrane eigenmode. Dividing this expression by G yields the responsivity to absorbed radiation, in Hz/W:

$$\Re_{abs} = \frac{\alpha}{G} H_{th}(j\omega), \tag{7}$$

where $H_{th}(j\omega)$ is a one pole low-pass filter that accounts for the thermal response time of the resonator:

$$H_{th}(j\omega) = \frac{1}{1 + j\omega\tau_{th}} \tag{8}$$

The responsivity to the incident radiation intensity, $\Re$, is finally given by multiplying $\Re_{abs}$ by the membrane absorption coefficient, which, according to Kirchhoff's law, equals membrane emissivity:

$$\Re = \varepsilon_{\lambda,\theta}(\lambda, 0)\Re_{abs}, \tag{9}$$

where $\varepsilon_{\lambda,\theta}(\lambda, 0)$ is the spectral normal emissivity. As shown in [4] and [14], for the case of a plain freestanding SiN membrane, the spectral normal emissivity $\varepsilon_{\lambda,\theta}(\lambda, 0)$ and the angle-integrated spectral hemispherical emissivity $\varepsilon_{\lambda}(\lambda)$ can be approximated as equal.

In order to benchmark models given in [4], [11], we characterize 90 ± 1.7 nm thick SiN membranes with the following nominal side-lengths (L): 1.5 mm, 3 mm, 6 mm, and 12 mm. Once the internal oscillator of the lock-in is phase-locked to one of the membrane's eigenmodes, the membrane is intermittently exposed to our IR source at a rate of 4 Hz using the chopper system that blocks light for 90% of the cycle.

In FIG. 2 (a), we clearly resolve a resonance frequency shift of ~9 Hz for resonance mode (3, 4), which is centered at around 76 kHz, for a $L = 6$ mm membrane. This would correspond to ~1.4 μW of absorbed radiation according to Eq. (7), in cases where $\omega << \frac{1}{\tau_{th}}$. In FIG. 2 (b), we obtain a 0.006 Hz RMS residual frequency shift for mode (3, 4). This residual shift corresponds to a ~0.9 nW RMS sensor absorbed noise floor for a sensing bandwidth of 50 Hz, which is the lowest value achieved in this work.

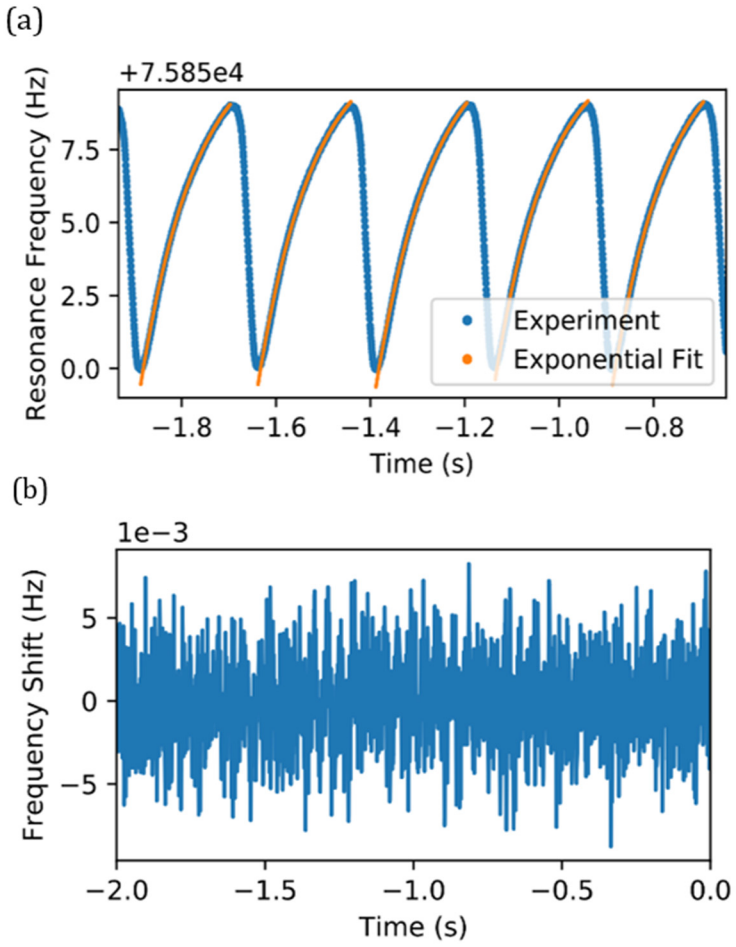

FIG. 2. (a) Frequency response of mode (3, 4) of an L = 6 mm membrane as it is intermittently exposed to an IR source. When the membrane is exposed to the IR source, the SiN stress is reduced, resulting in a lower resonance frequency. (b) Frequency shift for mode (3, 4) of a 6 mm membrane when the membrane is not exposed to radiation. Frequency fluctuations equate to 0.006 Hz RMS noise.

Changes in resonance frequency over time are fit with exponential curves, as seen in FIG. 2(a), to extract the characteristic thermal response time, τ_{th}, for multiple membrane dimensions. Accurate measurements of τ_{th} are ensured by configuring the PLL settings to a high bandwidth, such that the observed response time is limited solely by thermally-induced changes in the membrane resonance frequency. To determine these settings, the thermal time constant of various membranes were measured with multiple PLL bandwidths. As can be seen in FIG. 3 for the case of an $L = 6$ mm membrane, there are discrepancies in the value of the thermal time constant of the resonator at low PLL bandwidths. In this case, PLL

bandwidths less than 20 Hz were too slow to accurately measure the resonator's thermal time constant, whereas a plateau region can be seen when PLL bandwidths are ≥ 20 Hz. Considering this effect, the PLL bandwidth for all measurements is set to ≥50 Hz, which was verified to be fast enough for all membrane sizes and eigenmodes used in this work. The demodulator bandwidth of the lock-in amplifier is set to five times the PLL bandwidth, i.e., to 250 Hz.

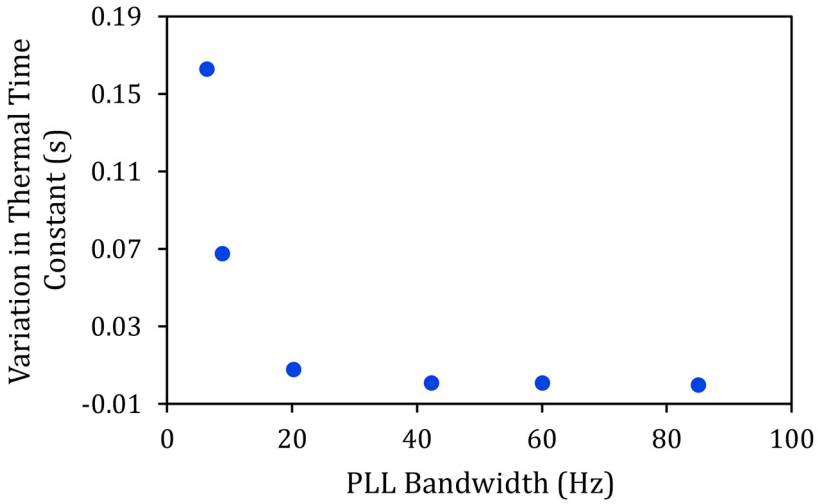

FIG. 3. PLL calibration. Increasing the PLL bandwidth until the measured response time shows a plateau region, indicating that the PLL bandwidth is sufficiently fast to measure the thermal response time of the membrane. These measurements were performed for mode (2, 2) of a SiN membrane with a 6 mm side-length.

Thermal time constants measured for multiple membrane sizes are shown in FIG. 4 (a) and show relatively good correspondence with both theoretical models [4], [11]. The model curves are generated assuming hemispherical emissivity (ε) of the 90 ± 1.7 nm thick SiN membrane is 0.097 in accordance with the emissivity model proposed in [4] and later corrected in [14]. Furthermore, different conductivities (k) are used when calculating the models to illustrate the effect of the large variability of values reported in literature [12], [13], [15] for this parameter. The value of k reported in the most recent comparative study (2.7

W/mK [13]) yields the best correspondence with both heat transfer models, which further validates these recent conclusions [13]. We therefore assume $k = 2.7$ W/mK for the remainder of this work. In FIG. 4 (b), we present the experimental data for additional eigenmodes and we note that higher mode orders have slightly lower thermal time constant values when compared to mode (1, 1). This can be attributed to the mode shape; wherein higher order modes have antinodes that are closer to the heat-dissipating Si frame.

In FIG. 4 (b), both models [4], [11] predict relatively accurate thermal time constants for small membrane sizes (L); however, we note a systematic difference between the two existing models in the radiation dominated regions ($L \geq 6$ mm). It appears that keeping only the first-order Taylor term for the membrane temperature profile, as in [11], can lead to an overestimation of τ_{th} as it cannot properly model a fully radiation-dominated profile that is expected to have a box-like shape—i.e., constant temperature almost everywhere, and sharp changes in temperature near the membrane edges. We note however that the over estimation of is modest (~20%) and, in most practical case, it is likely to be within the error margin resulting from other factors such as uncertainties in material constants (e.g., ρ, c_p).

We emphasize that no fit parameters are used in FIG. 4 (b) for matching measurement with theory curves. This indicates that the emissivity model for SiN proposed in [4] and [14], using the permittivity model given in [33], can likely be used with a high confidence level.

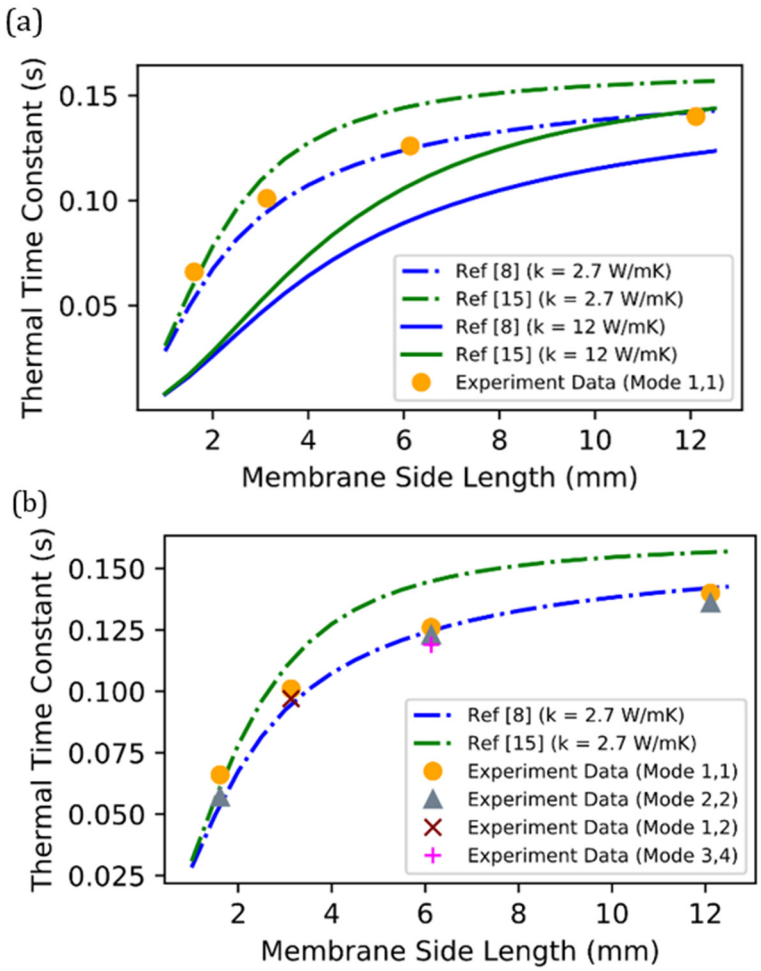

FIG. 4. Characteristic thermal response time of SiN resonators. (a) Comparison of experimental thermal time constant data to the Circular approximation model [4] and first order Taylor expansion approximation [11] for SiN membranes with side-lengths ranging from 1.5 mm – 12 mm. The emissivity for both models is calculated using the analytical model from [4] while the value for thermal conductivity is varied to show the impact different reported literature values have on the models. (b) Additional vibration mode measurements compared with thermal time constant models from [4], [11] assuming the most recent literature value for thermal conductivity (k = 2.7 W/mK [13]) and ε = 0.097. A radiation dominant region can be seen for membrane side lengths $\gtrsim$6 mm. For readability, only averaged measurements for multiple experimental trials are plotted on both figures. Error bars have been included to account for measurement repeatability, but the standard deviation values (on the order of 0.01 mm [x-axis] and 0.001 s [y-axis]) are too small to be visible.

6.5 Thermal Fluctuation-Induced Frequency Noise

Armed with our experimentally validated thermal transport model, we can now derive expressions for frequency noise and for noise equivalent power (NEP) resulting from thermal fluctuation noise in frequency-shift based SiN radiation sensors. We also analyse the contribution of thermal fluctuation noise relative to others—namely thermomechanical noise and experimental detection noise—that have been more extensively discussed in previous work [16]–[18], [25].

Thermal fluctuation noise results from random energy exchanges between the resonator and its surrounding environment and therefore depends on the thermal conductance (G) of the structure. These exchanges affect the resonator temperature, which in turn results in resonance frequency shifts. We can express the fractional frequency ($y = \frac{\Delta f}{f}$) fluctuation power density spectrum due thermal noise by multiplying the temperature noise spectrum (S_T, in K^2/Hz) [2], [19] by the normalized temperature sensitivity α^2/f_r^2:

$$S_{y,th}(\omega) = S_T(\omega)\frac{\alpha^2}{f_r^2} = \frac{4k_B T^2}{G}|H_{th}(j\omega)|^2\frac{\alpha^2}{f_r^2}\,, \tag{10}$$

where k_B is the Boltzmann constant. In turn, by combining this noise density function with the sensor responsivity [Eq. (9)], we can express the sensor noise equivalent power due to thermal fluctuation as:

$$NEP_{th} = \frac{\sqrt{S_{y,th}}f_r}{|\Re|} = \frac{\sqrt{4k_B T^2 G}}{\varepsilon_{\lambda,\theta}(\lambda,0)}, \tag{11}$$

Eq. (11), combined with the expression of G given in Eq. (4), provides a closed-form expression for the fundamental NEP limit of drumhead resonators when used as thermal radiation sensors. Note that when calculating G for use in Eq. (11), the area A must account for both sides of the membrane (i.e., $A = 2L^2$) unless surface functionalization allows for radiative coupling solely on the front surface. Care must also be given not to confuse spectral normal emissivity $\varepsilon_{\lambda,\theta}(\lambda,0)$ with the total hemispherical emissivity ε, especially in cases,

such as for SiN, where the former is strongly wavelength dependant [4], [14] (i.e., the gray body approximation does not apply).

We also note that Eq. (11) reduces to the classical fundamental detectivity limit of bolometers in the idealized case of a front-side coupled membrane ($A_{tot} = A_{front} = L^2$) with perfect absorption ($\varepsilon_{\lambda,\theta} = \varepsilon = 1$) and $x_{rad} = 1$ [1]:

$$D^*_{th} = \frac{\sqrt{A_{front}}}{NEP_{th}} = (16 k_B T^5 \sigma_{SB})^{-\frac{1}{2}}, \tag{12}$$

which is approximately $1.8 \times 10^{10} \frac{cm\sqrt{Hz}}{W}$ at $T = 300\ K$.

Obviously, other sources of noise must be accounted for in practical applications and thermomechanical noise is often the dominant one as indicated in [16]–[18], [25]. The spectral density of frequency noise induced by thermomechanical fluctuations is given by [16], [17]:

$$S_{y,tmech}(\omega) = \frac{k_B T}{m_{eff} \omega_r^3 Q a_{rss}^2} |H_{tmech}(j\omega)|^2, \tag{13}$$

where Q is the quality factor of the resonator, m_{eff} is the effective resonator mass, ω_r is the angular resonance frequency, and a_{rss} is the amplitude of the resonator motion in steady state. $H_{tmech}(j\omega)$ denotes the resonator transfer function, which is a one-pole low pass filter similar to Eq. (8) but with a characteristic resonator time constant $\tau_{mech} = Q/(\pi f_r)$ instead of the thermal time constant (τ_{th}). Minimization of thermomechanical noise is usually achieved by using a driving amplitude at the onset of nonlinearity [26]:

$$a_{rss} = a_{crit} = 0.56 \frac{L}{\sqrt{Q}} \sqrt{\frac{\sigma}{E}}. \tag{14}$$

Using the same approach as for NEP_{th}, we can derive an expression for thermomechanical NEP using $S_{y,tmech}$ in lieu of $S_{y,th}$ in Eq. (11), and the expression for a_{rss} given in Eq. (14):

$$NEP_{tmech} = \frac{3.57\, G(1-\nu)}{\varepsilon_{\lambda,\theta}(\lambda,0)\ \alpha_T L}\sqrt{\frac{k_B T\sigma}{m_{eff}\omega_r^3 E}}\frac{|H_{tmech}(j\omega)|}{|H_{th}(j\omega)|}. \quad (15)$$

Another noise source that affects sensing performance is detection noise. This noise source encompasses contributions from the readout system, signal amplification, membrane transduction, and is therefore specific to each experiment. A convenient way of expressing detection noise is to quantify its magnitude relative to thermomechanical noise [16], [18]:

$$S_{y,det}(\omega) = \kappa_d^2 \frac{k_B T}{m_{eff}\omega_r^3 Q a_{rss}^2}, \quad (16)$$

where κ_d is a dimensionless scaling parameter that indicates whether the background detection noise is sufficiently low for resolving thermomechanical displacement fluctuations (i.e., if $\kappa_d < 1$). Measurements of κ_d are presented in supplementary section S1.

Within the prospect of realizing radiation sensors operating at the fundamental detectivity limit set by Eq. (12), it is insightful to evaluate the relative contribution of NEP_{th} relative NEP_{tmech}, which commonly dominates frequency noise in nanomechanical resonators [16]–[18], [25]. We explore the relative contribution of NEP_{th} by defining the dimensionless ratio η:

$$\eta = \frac{NEP_{th}(\omega)}{NEP_{tmech}(\omega)} = \left(\frac{S_{y,th}}{S_{y,tmech}}\right)^{1/2}$$
$$= \frac{0.56\alpha_t L}{(1-\upsilon)}\sqrt{\frac{m_{eff}\omega_r^3 T E}{G\sigma}}\ \frac{|H_{th}(j\omega)|}{|H_{tmech}(j\omega)|}\ . \quad (17)$$

By evaluating η (see Fig 5) for parameters of a typical large area membrane ($L = 6$ mm) used in this work, we surprisingly find that thermal fluctuation noise can dominate over thermomechanical noise (i.e., $\eta > 1$) in large area SiN membranes. In Fig 5 (b), we note that thermal fluctuation noise can even dominate for membrane sizes down to 100 μm if we consider driving the commonly employed mode (2, 2) at the onset of non-linearity, with a typical Q-factor of 1 million. Frequency noise dominated by thermal fluctuation noise is in striking contrast with recent work on frequency noise in SiN string resonators, which clearly

demonstrated thermomechanical fluctuation-dominated behaviour [18]. Our current findings do not contradict this recent study [18], for which the ratio $m_{eff}/G\sigma$ was low due to the small size of the string resonator and the use of high-stress stoichiometric SiN as the resonator material. Large portions of this study [18] were also conducted for driving amplitudes much smaller than a_{crit} , thus increasing the relative contribution of thermomechanical noise. In Fig 5 (a), we also plot the actual predicted NEP values by considering $\varepsilon_{\lambda,\theta}(\lambda, 0) \approx 0.4$ to illustrate the performance of the membrane at $\lambda \approx 12$ µm, which is the maximum sensitivity wavelength of a SiN membrane [14]. We note that NEP_{th} ($\sim 4.1 \times 10^{-11}$ W/$\sqrt{Hz}$) dominates especially at frequencies greater than $\pi f_r/Q$ (vertical yellow dashed line), i.e., where the thermomechanical noise is filtered out by the system mechanical response time.

Thermal fluctuation-dominated frequency noise, as demonstrated in **Error! Reference source not found.**Fig 5 (a), is important as it could potentially enable thermal radiation sensors operating at the never achieved fundamental detectivity limit set by Eq. (12). In principle, doing so would only require functionalizing the membrane front side to become a perfect radiation absorber (i.e., $\varepsilon_{\lambda,\theta} = \varepsilon = 1$) and to thermally isolate the backside (i.e., $\varepsilon_{\lambda,\theta} = \varepsilon = 0$), while not deteriorating the membrane mechanical properties.

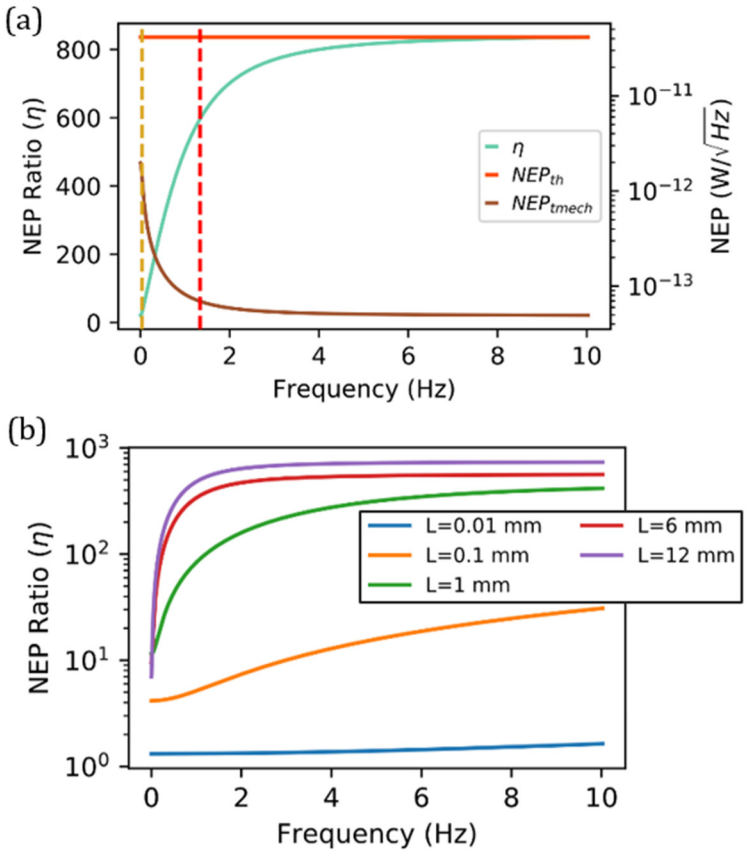

FIG. 5. Ratio of thermal NEP to thermomechanical NEP. (a) NEP for a typical membrane from this work (d = 90 nm, L = 6 mm, $Q \approx 10^6, \sigma = 100$ MPa), which is theoretically dominated by thermal noise. Membrane mode (3,4) ($f_r \approx 76$ kHz) and critical amplitude actuation are considered in this case. The red dashed line represents the bandwidth imposed by the thermal time constant of the membrane ($1/2\pi\tau_{th}$) while the yellow dashed line represents the resonator mechanical bandwidth ($1/2\pi\tau_{mech}$). (b) NEP ratio for additional membrane side-lengths (L = 0.01 mm, 0.1 mm, 1 mm, 6 mm, 12 mm). Here we can see thermal fluctuation noise can dominate even with smaller non-radiation dominant membrane sizes.

In a practical situation, it is also imperative to consider noise after processing by the frequency tracking experimental apparatus (a digital PLL in our case). NEP values presented in Fig. 5 (a) only include intrinsic resonator noise and therefore exclude this contribution. As demonstrated in [16]–[18], PLL frequency tracking can increase noise by orders of magnitude, especially if the PLL bandwidth (50 Hz in the present example) is significantly greater than the resonator mechanical bandwidth ($1/2\pi\tau_{mech} \approx 0.03$ Hz in the present case). For this reason, accurately predicting experimental noise must account for loop dynamics by

following the procedure outlined in [16], [17]. Our experimentally measured frequency noise (6×10^{-3} Hz RMS, see FIG. 2 b) is good example, being ~3 orders of magnitude greater than the frequency noise predicted by Eq. (10), (13) if we were to simply integrate these expressions over the 50 Hz PLL bandwidth. Doing so underestimates noise in the system by predicting values on the order of $\sim 10^{-6}$ Hz RMS. In contrast, considering the complete PLL loop dynamics along with detection and thermomechanical noise (see supplementary information S1) gives a better estimation of our experimentally measured noise.

6.6 Conclusion

In the first portion of this work, after comparing two recently proposed models for the thermal response time in SiN resonators [4], [11], we find that they both correspond relatively well with experimental results at small membrane sizes (i.e. non-radiation dominant resonators). When using the most recent value for thermal conductivity [13] and the analytical emissivity model from [4], [14] we see that the circular approximation model for calculating the thermal time constant more closely corresponds with the experimental data presented than the Taylor approximation model for membrane sizes ≥ 6. However, difference between the two models is modest and would likely be acceptable for most applications.

Secondly, using our experimentally validated heat transport model, we show that thermal fluctuation noise can often dominate intrinsic frequency noise in both large and small area membranes. However, experimentally verifying this is currently not possible due to the unknown effect of our PLL frequency tracking scheme on thermal fluctuation noise. While thermomechanical and detection noise have been analyzed in the context of PLL frequency tracking [16]–[18], the same analysis currently does not exist for thermal fluctuation noise. Performing this analysis is the logical next step to our work. Ultimately, a complete understanding thermal fluctuation induced frequency noise could lead to the design of

radiation sensors achieving the fundamental detectivity limit of bolometric thermal radiation sensors experimentally.

6.7 Supplementary Information

6.7.1 PLL Noise Analysis

The measured experimental noise in the main text (main text Fig. 2 b), is higher than predicted by our equations for the intrinsic resonator noise (Eq. 11, 15) due to the use of a PLL frequency tracking scheme. Such behaviour is expected and predictable using the theory given in [16], [17], and is especially pronounced for PLL bandwidths that are higher than the resonator bandwidth [$BW = (\pi f_r)/Q$]. High PLL bandwidths (~50 Hz) are required in our case for accurately characterizing our membrane thermal response time (see main text Fig. 3).[16], [18] Incorporating PLL loop dynamics into our noise analysis is possible by computing the predicted Allan Deviation due to thermomechanical and detection noise as given in [16]–[18]:

$$\sigma_y(\tau) = \frac{2}{\sqrt{\pi}\tau}\left[\int_{-\infty}^{+\infty} \frac{\left[\sin\left(\frac{\omega\tau}{2}\right)\right]^4}{\omega^2} S_y(\omega)\, d\omega\right]^{\frac{1}{2}}, \tag{S1}$$

where τ is the integration time and $S_y(\omega)$ is the spectral density of the fractional frequency fluctuations. Using Eq. (13) and (16) from the main text, the frequency noise from thermomechanical and detection noise is

$$S_y(\omega) = \frac{k_B T}{m_{eff}\omega_r^3 Q a_{rss}^2} |H_{tmech}^{PLL}(j\omega)|^2 + \kappa_d^2 \frac{k_B T}{m_{eff}\omega_r^3 Q a_{rss}^2} |H_{det}^{PLL}(j\omega)|^2, \tag{S2}$$

where H_{tmech}^{PLL} and H_{det}^{PLL} are transfer functions for thermomechanical noise and detection noise in a closed-loop system [16], [17]:

$$H_{tmech}^{PLL}(s) = \frac{\left(sK_p + K_i\right)H_L(s)}{s^2 + \frac{s}{\tau_{mech}} + \left(sK_p + K_i\right)H_L(s)}, \tag{S3}$$

$$H_{det}^{PLL}(s) = \frac{1}{H_{tmech}(s)} \frac{\left(sK_p + K_i\right)H_L(s)}{s^2 + \frac{s}{\tau_{mech}} + \left(sK_p + K_i\right)H_L(s)}. \quad \text{(S4)}$$

In the above expressions, two transfer functions are applied: the resonator filter $H_{tmech}(s) = \frac{1}{1+s\tau_{mech}}$ and the demodulator filter $H_L(s) = \frac{1}{1+s\tau_{demod}}$. Also introduced are the loop controller parameters K_p (proportional) and K_i (integral), which are calculated as a function of the PLL bandwidth [16], [17]:

$$K_p = \omega_{PLL}\,, \qquad K_i = \frac{\omega_{PLL}}{\tau_{mech}} \quad (S5)$$

Note that Eq S1-S5 do not include thermal fluctuation-induced frequency noise $S_{y,th}(\omega)$ because a transfer function $H_{th}^{PLL}(s)$ for this noise term is unknown to the authors. As stated in the conclusion of our manuscript, deriving such term and studying thermal-frequency fluctuation in closed loop would be the logical next step to our work.

In FIG. S6 (a) we show a 5-minute frequency noise measurement (similar to Fig 2b of the main text, but for a longer acquisition time), which is then converted to an Allan deviation and plotted (FIG. S6 (b)) with the model detailed above. In FIG. S6 (b), we compare the experiment data with the Allan deviation for a 0.03 Hz PLL bandwidth, which would be optimally matched to the mechanical bandwidth of the resonator, and for a 50 Hz PLL bandwidth, which was the bandwidth used in our experiments to resolve the thermal response time. We can clearly see an increase in system noise by ~3 orders of magnitude for our 50 Hz PLL bandwidth, compared with the noise that would be expected if we had matched our PLL bandwidth to the resonator bandwidth. In the latter case, the Allan deviation closely follows the asymptotic behaviours for thermomechanical and detection noise (i.e., no extra noise is expected above the predictions of Eq. 13, 16). The noise present in our experiment more closely corresponds

to the theoretical model for the 50 Hz PLL bandwidth. This supports the case that the higher noise levels seen experimentally are due to the use of a high PLL bandwidth. At $\tau \approx 0.03$ s, there is an increase in the experimental Allan deviation, which is not present in the model. The exact source of this increase is still unknown; however, a possible cause could be noise introduced while driving our membrane near the onset of nonlinearity. At higher integration times, noise due to drift dominates our membrane resulting in further deviation from the theoretical model, as is commonly seen experimentally [18].

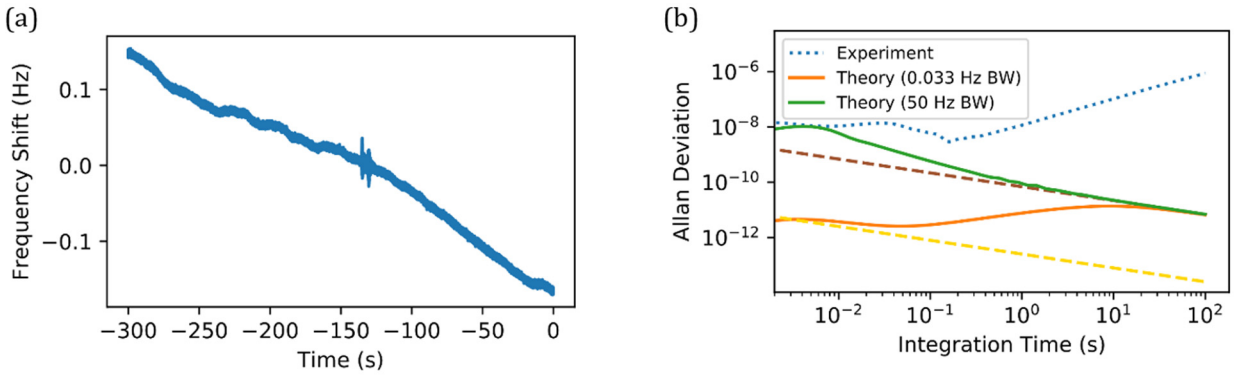

FIG. S6*. (a) Frequency noise trace over a duration of 5-minutes for mode (3, 4) of an $L = 6$ mm membrane. (b) Theoretical Allan Deviations (solid lines) and experimental (dotted line) Allan deviations of mode (3,4) of an $L = 6$ mm membrane. Increasing the PLL bandwidth from 0.03 Hz to 50 Hz results in an increase in the Allan deviation by ~3 orders of magnitude. For a PLL bandwidth matched to the resonator bandwidth (0.03 Hz) the Allan deviation follows the detection noise asymptote (yellow dashed line) and the thermomechanical noise asymptote (brown dashed line)*

To calculate the detection noise ($S_{y,det}$, Eq. 16 in main text) in our setup and generate the plot seen in FIG. S6 (b), we measured the dimensionless parameter κ_d, which indicates the relative contributions of thermomechanical and detection noise. This parameter was determined experimentally by measuring the power spectral density (PSD) over 100 Hz bandwidth near the resonance peak of the membrane when no drive was provided by the shear piezo in our setup. Under these conditions we can still see a peak in the PSD at the resonance frequency of our resonator due to thermomechanical noise. Taking the ratio between the $\sqrt{PSD}$ of the background detection noise (red dashed line in Figure 4.6) and the

$\sqrt{PSD}$ of the resonance peak induced by thermomechanical noise (green dashed line in Figure 4.6) results in a κ_d value of 0.006.

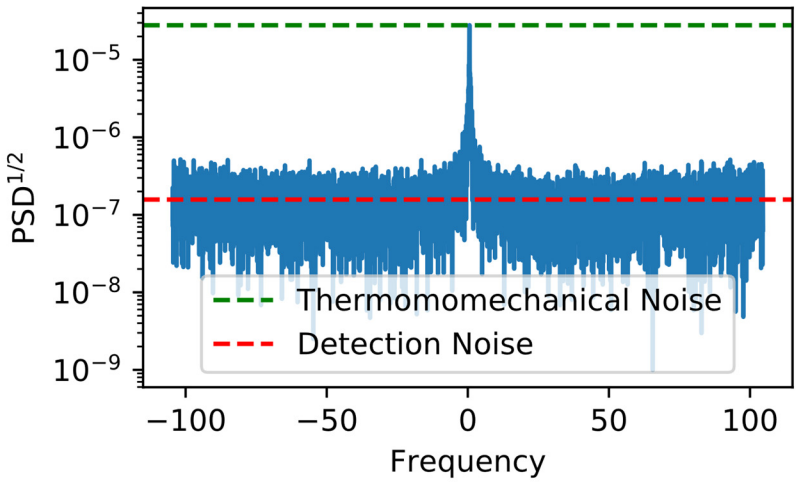

FIG. S7*. Measurement of detection amplitude noise relative to thermomechanical noise (κ_d). Spectrum over 100 Hz BW near the resonance peak of the membrane is measured when no actuation is provided by the shear piezo (i.e., resonator motion is a result of random motion of particles around and within the membrane). The $\sqrt{PSD}$ ratio between the background detection noise (red dashed line) and the resonance peak caused by thermomechanical noise (green dashed line) yields κ_d = 0.006.*